UNIVERSITEIT TWENTE

MASTER'S THESIS

SOFT MATTER, FLUIDICS AND INTERFACES

The effect of membrane topology features on ion transport phenomena

Author:
Michel Schellevis

Committee:
Prof. Dr. Ir. R.G.H. Lammertink
Dr. J.A. Wood
A.M. Benneker, MSc
Dr. Ir. W.M. de Vos

April 14, 2017

UNIVERSITEIT TWENTE.

Abstract

The formation of electroconvective vortices enhances ion transport through ion-exchange membrane to the overlimiting current region. A tangential electric field acting on an excess of charge initiates electroconvection. The introduction of heterogeneities on the membrane surface ensure such electric field. Previous work have shown an increase in ion transport properties with the introduction of extrusions on the surface of the membrane. This research provides an experimental and numerical investigation to extend our knowledge on the effect of membrane topology features. Electrical characterization of the system is combined with fluorescence lifetime imaging microscopy to quantify local ion concentration profiles. It is found that the implementation of structures on the membrane surface seems to enhance ion transport. Local ion concentration is quantified and shows a linear concentration profile perpendicular to the membrane, flattening out near the membrane, indication the formation of microvortices adjacent to the membrane surface.

Contents

List of Figures

List of Tables

1 Introduction

Electrodialysis (ED) is a membrane separation technique used to desalinate salt water.[1] In regions where sea water is the only reliable water source, ED is an interesting technique to produce drinking water. It uses ion-exchange membranes to separate species with a different charge under influence of an electric field. An increase in potential will result in a higher ion flux until ion concentration polarization limits ion transport. This is the limiting current density and industrial processes operate slightly below this point. A further increase in potential will not result in a higher ion flux until a certain threshold potential. After this threshold, the ion flux starts increasing again, which is called overlimiting current (OLC). Operating in this regime would not be beneficial from an energy point of view, however the decrease in required membrane surface area lowers the capital investment costs.[1, 2]

Electroconvection has been identified as a major contributor to OLC, initiated by a tangential electric field acting on a space charge.[2, 3] Certain modifications of the membrane surface can bend the electric field in such that a tangential component is ensured.[1] A previous study has shown an enhancement of ion transport by the implementations of extrusions on the membrane surface.[4] This research follows up on this work studying the effect of membrane topology features experimentally and numerically. The goal of this research is to obtain more insight in how membrane topology features influence ion transport near an ion-selective interface.

The experiments will be carried out in a transparant PMMA cell with the possibility to conduct electrochemical experiments and fluorescence lifetime imaging microscopy (FLIM) measurements. With electrochemical experiments the influence of membrane topology on ion transport can be investigated, while FLIM will be used to quantify the local ion concentration close to the membrane surface. Numerically the system can be described by a Poisson-Nernst-Planck with Navier-Stokes framework. The numerical model enables the analysis of more complex membrane topology features to eventually find the optimal membrane surface topology.

This thesis starts with a theoretical background of electrodialysis, concentration polarization and OLC in *Chapter 2*. Electrochemical and fluorescence lifetime imaging microscopy experiments are carried out to investigate the effect of membrane technology features experimentally. Aspects regarding the experimental work is explained in *Chapter 3*, whereas *Chapter 4* provides the he mathematical framework used for the 2D numerical model. The results of the experiments and simulations are interpreted and discussed in *Chapter 5*. Finally, *Chapter 6* provides the conclusions of this research and gives recommendations for future work on this topic.

2 | Background

This chapter provides a theoretical background to this thesis. The starting point is the basics of electrodialysis, which is the technique that forms the basis. First, the principles of electrodialysis and its major applications will be explained. Ion-exchange membranes are crucial components of the electrodialysis system, section 2.1.3 is dedicated to that. Next, concentration polarization is explained and finally the interesting phenomenon of overlimiting current will be discussed in detail.

2.1 Electrodialysis

Electrodialysis (ED) is a separation technique in which a gradient in electric potential is the driving force to separate species with a different charge. When an electrical potential is applied between two electrodes, the species with a positive charge (cations) will migrate towards the (negatively charged) cathode and negatively charged (anions) species will migrate towards the (positively charged) anode. Ion-exchange membranes (IEMs) play an important role in the system since they are able to retain species with one charge and pass through species with the opposite charge.[5, 6]

2.1.1 Principles

Figure 2.1 shows the principles of ED. In an ED system, cation-exchange membranes (CEMs) and anion-exchange membranes (AEMs) are placed in alternating series. An electrolyte solution is pumped through the compartments between the membranes and an electrical potential between the electrodes is applied. The cations migrate towards the cathode through the CEM but are retained by the AEM. The opposite holds for the anions, they pass through the AEM towards the anode but are retained by the CEM. This results in a concentrated compartment and a diluted compartment in alternating series. For industrial size electrodialysis, about 100 to 200 unit cells, as illustrated in Figure 2.1, are placed in series between the electrodes to increase the capacity of one electrodialysis stack.[5–7]

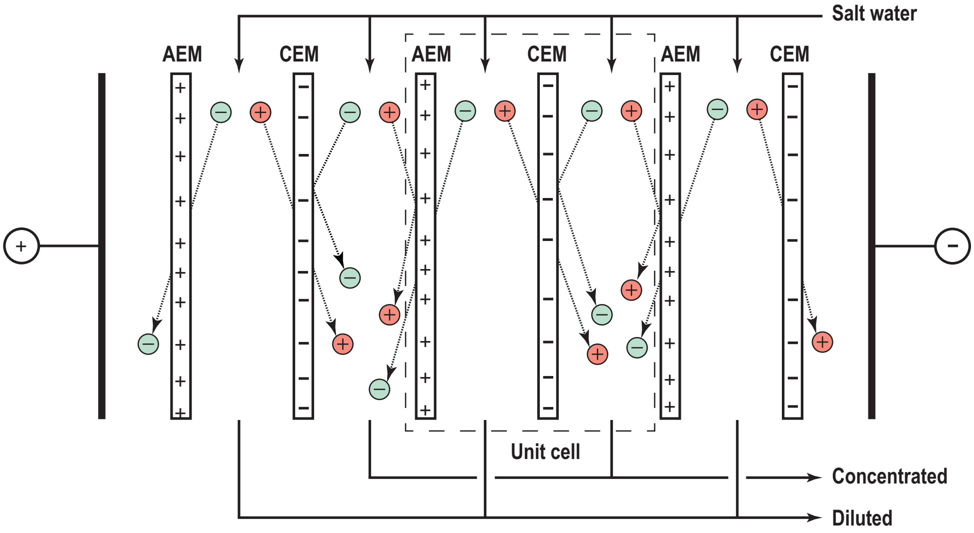

Figure 2.1 – Principles of electrodialysis. Salt water is fed to the compartments and a electrical potential is applied between the electrodes. Cations move towards the cathode and anions move towards the anode. The unit cell gives a repeating unit, that can be placed in series to increase the capacity of one module.[5]

2.1.2 Applications

Since the 1950s, ED has been used for the production of drinking water from brackish water sources. The technique can be considered as mature and over the years it has been modified and improved for a multitude of applications.[6] Still, the major application of ED is the desalination of brackish water to produce potable water. A conventional ED system as schematically shown in Figure 2.1 is used. Brackish water has a salinity of 20 to 200 $\mathrm{meq\,L^{-1}}$ (where meq is based on the valence of the ions), which is significantly lower than sea water (600 $\mathrm{meq\,L^{-1}}$).[8] With ED this has to be decreased to 10 $\mathrm{meq\,L^{-1}}$ to make it potable. For this application, ED has to compete with reverse osmosis. The advantages of electrodialysis is the little amount of required pre-treatment. Membrane fouling is usually a major issue in membrane processes. In ED however, the deposited particles carry a charge, therefore it is relatively easy to remove them by simply reversing the electric field. Other advantages are a good mechanical and chemical stability of the membranes and the possibility to increase the operating temperature up to 50 °C. The major drawback of ED is the inability to remove non-charged species. Contaminants such as viruses, bacteria and organic contaminants will not be removed. Overall, ED is economically favourable over reverse osmosis at relatively low salt concentrations in the feed (1000 to 5000 mg/L) and small to medium plant sizes (~100 to 20 000 $\mathrm{m^3/d}$).[1, 5, 6, 8]

The same ED concept can be used in other applications, for example demineralization of boiler feed, waste water treatment and the recovery of metals and acids. Another application is to concentrate sea water before evaporation and crystallization to reduce the energy costs. With ED an 18 to 20 wt % concentrated salt solution of can be achieved.[6]

Modifications of the system have let to the developement of other processes based on ED. The production acids and bases using bipolar membranes, continuous electrodeionization, capacitive deionization and reverse electrodialysis to produce energy are a few examples were ion-exchange membranes play an important role. This research can have direct implications for these applications. [6, 7, 9–11]

2.1.3 Ion-exchange membranes

An essential aspect of ED are ion-exchange membranes. In order to perform well in ED processes, they should have a [1, 12, 13]

- *high permselectivity* – only counterions should be able to permeate the membrane
- *low electrical resistance* – enabling the highest possible permeation of counterions
- *good mechanical stability* – they should be able to withstand the operating circumstances
- *good form stability* – when switching from a diluted to a concentrated solution, the membrane should not shrink or swell
- *high chemical stability* – the membrane should be stable in the whole pH range
- *reasonable costs* – a low production cost of the membrane makes it more economically viable for industrial scale applications

In order to fulfil the high permselectivity criterion, either positively charged ions or negatively charged ion should be able to permeate the membrane. This is achieved by the introduction of groups with a fixed charge in the structure of the membrane. Then only ions with the opposite charge are able to get in the vicinity of the membrane surface, hence, be able to diffuse through the membrane. This concept is called Donnan-exclusion.[13] IEMs can be classified in three groups: (1) cation-exchange membranes, (2) anion-exchange membranes and (3) bipolar membranes.[1] Examples of the three types of IEMs can be found in Appendix A.

Optimization is difficult as parameters defining the properties of the membrane can have opposing effects. For instance, crosslinking of the base polymer increases the mechanical stability, but also increases the electrical resistance. In general, the polymer matrix determines the mechanical, chemical and thermal stability and the fixed ionic groups determines the permselectivity and electrical resistance.[13]

2.2 Concentration polarization

Concentration polarization (CP) is an inevitable phenomenon in membrane processes, limiting mass transfer through the membrane.[14] Components with a high permeability will be depleted in the feed solution close to the membrane, whereas components with a low permeability will concentrate in the feed solution near the membrane. The CP mechanism for ED differs from pressure driven membrane processes. Positive ions and negative ions migrate in opposite directions. Under an applied potential, cations will move through the CEM and anions move in opposite direction. Also according to the electroneutrality principle the cation and anion concentration has to be equal. Therefore for every cation passing through the membrane an anion has to move away from the membrane. Similar behaviour occurs at the AEM, leading to a depletion of ions at the membrane surface in the dilute cell and a concentration of ions at the membrane surface in the concentrate cell. At elevated driving forces, the depletion of ions near the membrane surface of the depleted compartment limits the ion transfer. At a certain point diffusion from the bulk towards the membrane surface is not able to compensate for the ion flux through the membrane.[3, 15]

Figure 2.2 is a typical result when plotting the ion flux, given as current density, against the driving force, the potential. Three regimes can be identified. A linear Ohmic region at low current, the slope of the curve gives the electrical resistance of the system. Then CP limits the ion flux through the membrane resulting in a plateau region. The current density where it sets in

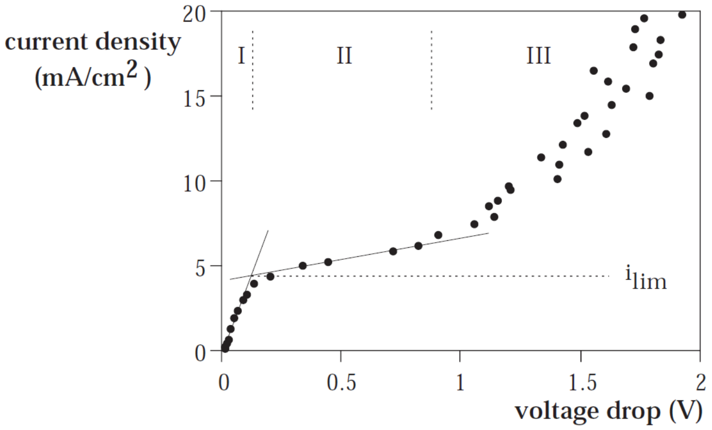

Figure 2.2 – Typical i-V curve of an ion-exchange membrane[16]

is called the limiting current density. After a threshold potential, the current density increases again. This phenomenon is called the overlimiting current.[16] According to the CP theory it is not possible to have a higher ion flux than at the limiting current density due to diffusion limitations. Over the years multiple mechanisms have been described to explain the observation of current at overlimiting conditions.[2, 3]

2.3 Overlimiting current

Operating in the overlimiting current (OLC) region can be interesting for ED processes. An increase in current density lowers the required membrane surface area, decreasing capital investment costs. From an energy point of view this would not beneficial since it requires relatively more energy to operate in the OLC region.[2]

2.3.1 Water dissociation

During experiments with AEMs, a pH change was observed.[16] This led to the idea that protons and hydroxide-ions generated at the membrane surface at elevated potentials are responsible for the additional charge transfer. However, it has been shown that only at the AEM some water dissociation occurs, accounting for less than 3 % of the total ion flux through the membrane.[3, 16, 17]

The difference in behaviour between AEM and CEM can be found in the ion-exchange groups. Only weak ion-exchange groups catalyse water dissociation. In principle only strong ion-exchange groups, sulphonic acid and quaternary amide, are present in the most common membranes. Probably some of the quaternary amide groups are converted to tertiary amides groups, enhancing water dissociation. Sulphonic acid groups are ‘stable’ and therefore no water dissociation is possible, unless there are metal ions present at the CEM surface. Metal ions like Al^{3+}, Co^{2+}, Mg^{2+} and Mn^{2+} are able to form hydroxides that can catalyse severe water dissociation. This concludes that water dissociation is most likely not the cause of OLC. It can only have a significant contribution in the presence of groups catalyzing water dissociation.[3, 18–20]

There is a second mechanism based on water dissociation that enhances ion-transport: migration current exaltation. When a charge appears at a membrane surface similar to the fixed charges of the membrane it attracts salt ions from the bulk. For example the production of OH^- at a CEM surface due to water splitting, but also leaking of co-ions through the membrane. The increase in ion-transport as a result of this mechanism, also referred to as the Kharkats effect, is also not large enough to cause OLC.[2]

2.3.2 Coupled convection

IEMs, and in particular CEMs, do not lose permselectivity in the OLC regime. This directly means that all charge is still carried by counter ions. Somehow, more counter ions must be transferred to the membrane surface. Spontaneous convective mixing in the diffusion layer is suggested to be a powerful mechanism. Two different mechanisms for this coupled convection are considered, namely gravitational convection and electroconvection.[2, 3]

Gravitational convection

Gravitational convection arises as a result of buoyancy forces resulting from density gradients. These forces can have two origins: (1) a concentration gradient or (2) a temperature gradient. CP will cause a depletion of ions facing the dilute channel and a concentration of ions facing the concentrate channel. The resulting density gradient inside the channel possibly initiates gravitational convection. A temperature gradient may be established due to Joule heating.[21]

The effect of gravitational convection can be tested by changing the orientation of the setup in the Earth's gravity field. Buoyancy forces only arise when the density gradient points upwards. Experimental results show there is no influence of the earth's gravitational on the ion-transport. These experiments are carried out with 1 mm distance between the membranes. Increasing this distance will increase the buoyancy forces and might cause a gravitational force high enough to give a convective flux.[3, 21]

From a theoretical point of view, the Rayleigh number can be used. It gives the ratio between buoyancy forces and diffusive mass transport (Eq. (2.1)).

$$Ra = \frac{g\rho'\delta^3}{\nu D} \tag{2.1}$$

Only when the Rayleigh number is larger than 1000, it is possible for gravitational convection to destroy the diffusion boundary layer. A quick calculations shows that the Rayleigh number for typical ED systems is at least one order of magnitude lower.[3, 22]

All of the above concludes that gravitational convection is most likely not the origin of OLC. It can only contribute when the distance between the membranes is sufficiently large (which is often not the case).

Electroconvection

The second type of coupled convection is electroconvection, defined as: “non-gravitational free convection in macroscopic domains of the electrolyte solution, caused by the interactions of a self-consistent electric field with the corresponding space charge”.[3, 22] Some different types of electroconvection can be distinguished, although they all have the same above-mentioned principle.

Electro-osmosis is the movement of the electrical double layer (EDL) under the influence of a tangential electric field. In Figure 2.3 the EDL is shown. The EDL exists also in the absence of an electric field or a semi-permeable interface. A negatively charged surface attracts positive ions, which are immobilized at the wall, this is the Stern layer. In the adjacent layer, there is also an excess of positive ions, as they are attracted by the surface. This is called the Gouy-Chapman layer and both layers together form the quasi-equilibrium EDL.[23] When a tangential electric field is applied, the positively charged EDL moves towards the cathode dragging along the quasi-neutral bulk. This results in electro-osmotic flow.

Due to the fixed charges of an IEM, electro-osmosis can play a role in coupled convection. This type of electroconvection is also referred to as “electro-osmosis of the first kind”.[3]

An extended space charge region can also cause electroconvection. This mechanism is based on the same principle as electro-osmosis. At the surface of a CEM an EDL forms. An electric field is applied and ions are depleted from the region near the membrane surface (the EDL still exists). This leads to diffusion of cations to the membrane surface and a diffusion layer between the bulk and EDL, hence concentration polarization. Anions migrate in the opposite direction. At higher voltages, above the limiting current, the net flux of cations and anions from the depletion zone is not zero. The electroneutrality assumption does not hold: a region appears between the EDL and the diffusion zone where the cation concentration is higher than the anion concentration resulting in a non-equilibrium extended space charge region (ESC).[24]

In the presence of an electric field containing a tangential component, the movement of the ESC due this tangential force will result in the formation of vortices. When this movement of the fluid due to an excess of charge occurs in the vicinity of the membrane surface it is referred to as “electro-osmosis of the second kind”.[2, 24, 25] Also in the quasi-equilibrium bulk of the electrolyte, i.e. further away from the membrane, residual space charge can occur. Electroconvection due to the electric field acting on this charge is called “bulk electroconvection”.[2, 26, 27] This type of electroconvection is suggested to be the major contributor to the OLC phenomenon[2, 3, 24]

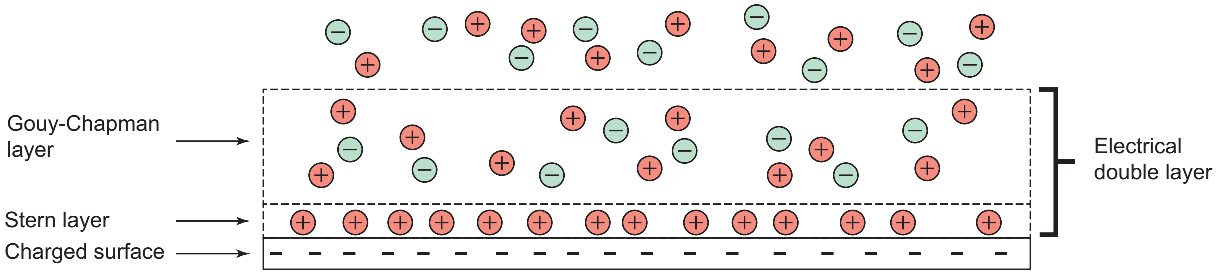

Figure 2.3 – Schematic representation of the electrical double layer. The surface is negatively charged. The Stern layer and Gouy-Chapman layer together form the electrical double layer (EDL).[23]

2.3.3 Vortex formation

The fluid velocity field near the ion selective interface has been visualized to investigate the influence of electroconvection on ion transport. This has been done by particle tracking; tracer particles are suspended in the electrolyte solution and, in theory, do not influence the fluid motion. A typical result is shown in Figure 2.4. Over time, electroconvective microvortices appear, mixing the diffusion layer and enhancing ion transport from the bulk to the membrane.[28, 29]

A tangential electric field is necessary to initiate electroconvective vortices. This can be achieved by implementing heterogeneities to the membrane surface, which will curve the electric field lines and result in a tangential component of the electric field. In Figure 2.4, however, the membrane surface is homogeneous but still electroconvective vortices form. Numerical solutions have shown that for sufficiently high voltages, the system becomes hydrodynamically unstable. Small velocity or concentration fluctuations can result in electrohydrodynamic turbulence.[2, 30]

The influence of OLC on the concentration profile near a ion-exchange surface is shown in Figure 2.5. In the first graph (Figure 2.5(a)), 'normal' CP is shown, corresponding to the Ohmic regime of the I-V curve (Figure 2.2). An EDL is formed at the membrane surface and diffusion is the dominant ion-transport mechanism. A further increase in potential results in the discussed overlimiting current and subsequent vortices. The concentration profile (Figure 2.5(b)) consists of four regions. The same two regions (EDL and diffusion layer) as in (a) still exist, although the concentration gradient in the diffusion layer is higher and hence also the ion flux is higher. As discussed, overlimiting current will cause an ESC adjacent to the EDL. Also a depletion zone with a flat concentration profile (so no diffusive transport) forms. In this depletion zone the convective vortices accommodate ion transfer. Figure 2.5(c) shows the development of the boundary layer as function of the current density. When the current density approaches the limiting current density, a depletion zone starts forming and vortices occur. With increasing current density the vortex size grows as well as the vortex speed, therefore also increasing the boundary layer. Starting off with a uniform concentration profile and operating at a constant current density above the limiting current density, it takes some time before ion depletion near the membrane sets in (Figure 2.5(d)). At first ($t = t_1$) diffusion is the main transport mechanism, then CP sets in and a depletion layer forms ($t = t_2$). Vortices grow over time and an expansion of the depletion zone occurs until a similar profile is obtained as in (c) ($t = t_3$). During this whole process, the width of the boundary layer is fixed.[31]

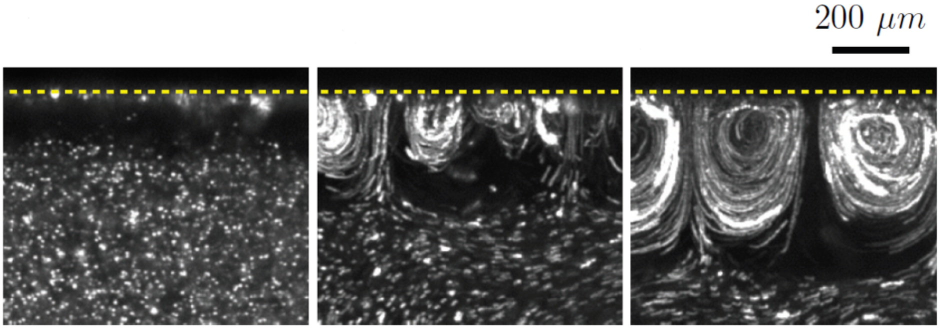

Figure 2.4 – Visualization of fluid movement near a CEM. A current density of 10 A/m^2 is applied. The dashed line represents the membrane surface. The snapshots are taken after 100 s, 220 s and 420 s from left to right.[29]

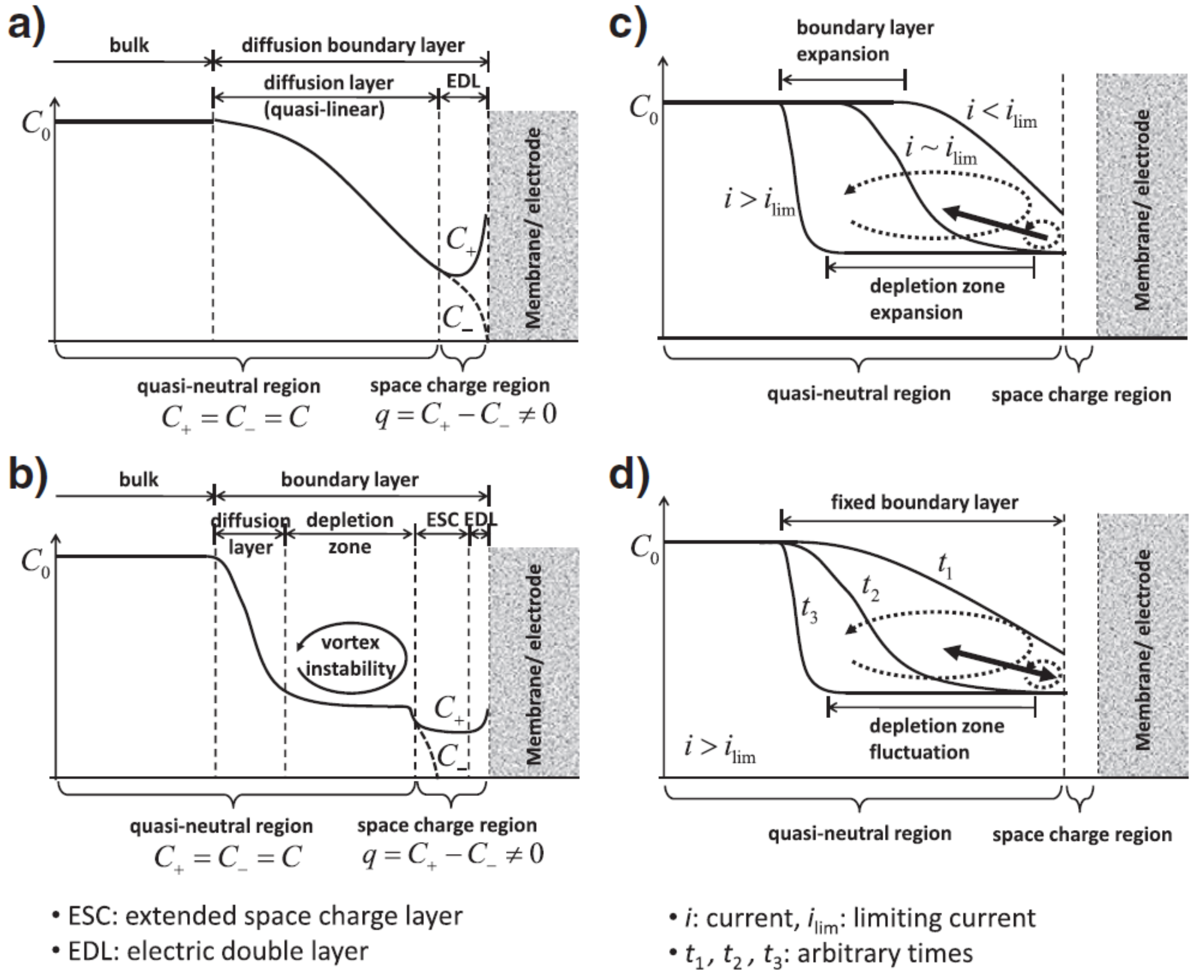

Figure 2.5 – Schematic anion and cation concentration profiles. In a) the concentration profile in the Ohmic region is given, whereas b) is in the OLC region. c) gives the concentration profile at current densities in the Ohmic, plateau and OLC regions. d) shows the development of concentration profiles over time for the OLC region.[31]

2.3.4 Membrane modifications

Microvortices near the membrane surface are kept responsible for OLC. A tangential electric field acting on an excess of charge initiates the formation of these electroconvective vortices. The implementation of heterogeneities to the membrane surface ensures the presence of a tangential component of the electric field, potentially decreasing the plateau length and increasing the ion flux at OLC conditions. Figure 2.6a shows the effect of a heterogeneous membrane surface on the electric field lines.[1, 2]

Examples of membrane surface heterogeneities are given in Figure 2.6. Alternating conductive and non-conditive surface[1, 2, 32, 33], chemical degradation of the membrane[34] and changing hydrophobicity of the surface[35] are examples of proposed methods.

A different approach is to change the shape of the membrane surface. Differences in electrical resistance between electrolyte and membrane will curve the electric field lines. A variety of membrane surface shapes are possible, such as a v-shape, pillars and line structures. [1, 4, 32, 33] Previous research has investigated the effect of line structures shown in Figure 2.6b. This resulted in a decrease in the electrical resistance of the system depending on the length of the extrusion.[4] This research aims to expand the knowledge on the influence of such topology features. Experimental research focuses on the enhancement of the ion flux, whereas fluorescence lifetime imaging microscopy can be used to quantify local ion concentration profiles. Numerically the research can be expanded to more complex membrane topology features, eventually to find the optimal membrane topology for electrodialysis processes.

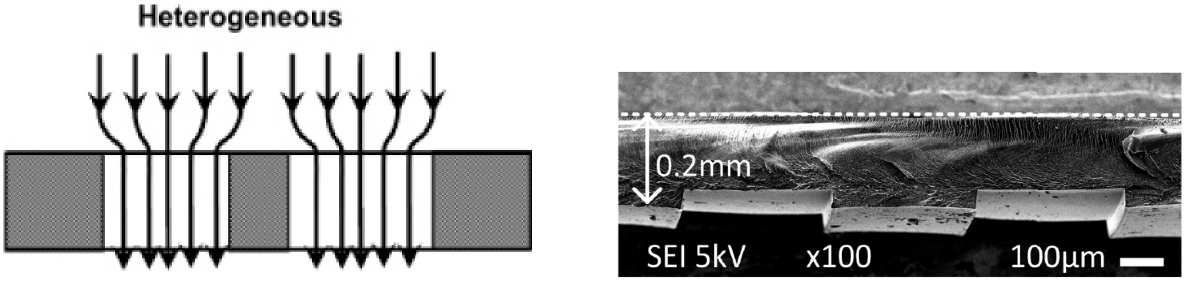

(a) Membrane surface modifications using alternating conductive and non-conductive surfaces.[3]

(b) Membrane surface modification using a structured membrane.[4]

Figure 2.6 – Illustration of membrane modifications to influence the onset and magnitude of electroconvection

3 | Experimental

The effect of membrane topology features on the electrokinetic and electrohydrodynamic behaviour near a cation-selective interface is investigated experimentally. Electrochemical measurements are carried out to investigate the electrical characteristics at various experimental conditions. Fluorescence lifetime imaging microscopy (FLIM) is used to quantify the ion concentration profile near the membrane interface. This chapter provides information about the experimental setup, properties of the used materials and a description of the experiments to be carried out.

3.1 Setup

Figure 3.1 shows the PMMA cell in which the experiments are conducted. A cation-exchange membrane is placed between the cathode and the anode. The surface area of the cathode ($52.6\,\mathrm{mm}^2$) is much larger than the membrane surface area ($13.5\,\mathrm{mm}^2$). This ensures concentration polarization to occur primarily at the membrane interface, while it is negligible at the electrode interface. A funnel shaped channel provides a homogeneous and perpendicular electric field prior to the membrane. This is also the reason why the cathode is placed further away from the membrane than the anode. A glass window is placed in front of the channel between the membrane and the anode. On this side of the membrane, the solution will be depleted and mass transfer is enhanced in the overlimiting current regime. The window enables the use of particle image velocimetry (PIV) and fluorescence lifetime imaging microscopy (FLIM).

A four electrode system is used to apply a potential and measure the resulting current. All electrodes are made of copper, with a 10 mM $CuSO_4$ electrolyte solution used during all experiments. This results in simple reactions at the electrodes, eq. (3.1). This means that copper is deposited at the cathode and consumed at the anode.[36]

$$\mathrm{Cu^{2+}(aq)} + 2\,\mathrm{e^-} \rightleftharpoons \mathrm{Cu(s)} \tag{3.1}$$

3.2 Materials

3.2.1 Electrolyte

The experiments are carried out with a $CuSO_4$ electrolyte solution. This is prepared by dissolving copper(II) sulfate pentahydrate ($CuSO_4 \cdot 5H_2O$) in deionized water (MilliQ). Copper sulfate dissociates into the divalent ions Cu^{2+} and ${SO_4}^{2-}$. The solution becomes slightly acidic, caused

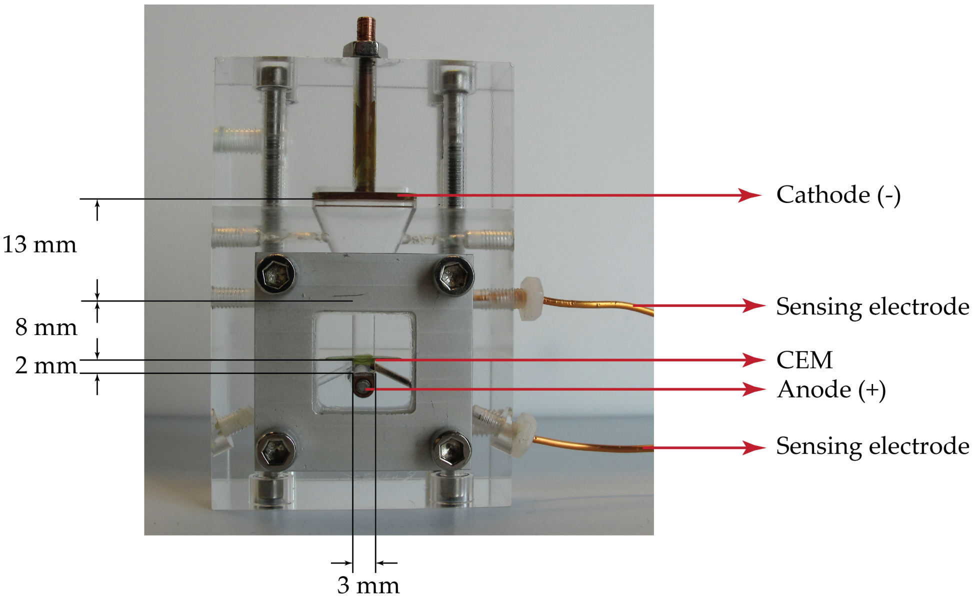

Figure 3.1 – The membrane test cell with the electrode connections and dimensions. The depth of the anode channel is 4.5 mm and the depth of the cathode channel is 4 mm.

by complex formation of Cu^{2+} with OH^- and some absorption of CO_2 from the atmosphere. For a 10 mM $CuSO_4$ solution, the pH is about 4.5.[4] This corresponds to a H_3O^+ concentration of 0.032 mM, which is negligible compared to the concentration of Cu^{2+} and ${SO_4}^{2-}$. Hence, the vast majority of the current in this system is transported by Cu^{2+}.

The conductivity of the solution as function of $CuSO_4$ concentration is determined. A 10 mM $CuSO_4$ solution has a conductivity of 1.47 ± 0.05 mS/cm. This is similar as previously reported.[4] More information about the calibration curve can be found in Appendix B.

The limiting current density (i_{lim}) can be calculated using eq. (3.2). At the limiting current density, the ion concentration near the membrane interface reaches zero and a linear concentration gradient is established. The average diffusivity is calculated by eq. (3.3) using $D_+ = 0.714 \times 10^{-9}$ m^2/s and $D_- = 1.065 \times 10^{-9}$ m^2/s.[37] An ideally permselective membrane will give a transport number at the membrane (t_m) of 1. In practice there will always be some permeation of co-ions. For this system the membrane transport number has been determined at 0.96.[4] The transport number of the bulk (t_b) is the ratio of cation and anion diffusion coefficients, $t_b = z_+D_+/(z_+D_+ + |z_-|D_-)$.

$$i_{\text{lim}} = \frac{zFD_{avg}}{t_m - t_b}\frac{c_0}{\delta} = 2.95 \text{ A/m}^2 \tag{3.2}$$

$$D_{avg} = \frac{(z_+ + |z_-|)D_+D_-}{z_+D_+ + |z_-|\,D_-} = 0.855 \times 10^{-9}\,\text{m}^2/\text{s} \tag{3.3}$$

Experiments using the same set-up and conditions as used here have shown a diffusion layer (δ) of ~1 mm.[4] With a valence number of 2 and the Faraday constant (9.65×10^4 C/mol), the limiting current density of this system is estimated at 2.95 A/m^2.

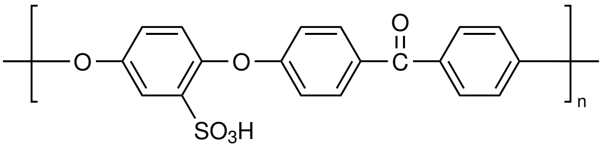

Figure 3.2 – Molecular structure of sulphonated poly(ether ether ketone) (SPEEK).[38]

3.2.2 Ion-exchange membrane

A CEM is used during the experiments. Hence, CP occurs on the anodic side of the membrane. The membrane is made of sulphonated poly(ether ether ketone) (SPEEK), the molecular structure is shown in Figure 3.2. In this study, the effect of membrane topology features with respect to overlimiting current (OLC) is investigated. Therefore, membranes are synthesized with structures shown in Figure 3.3. The gaps have the same length (L) as the elevated regions and are 50, 100, 200 and 800 µm wide.

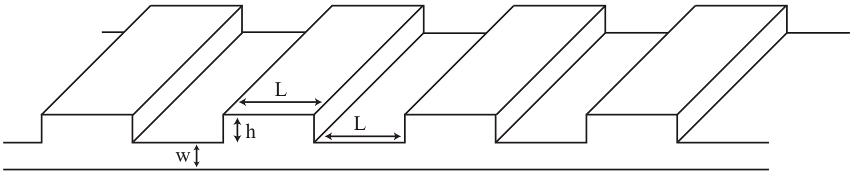

Figure 3.3 – Schematic drawing of the ion-exchange membranes. The extrusion always has the same length as the gap.

To synthesize the membrane a mold of the desired topology features is prepared in the clean room by means of dry etching. A solution of 20 % SPEEK in n-methyl-2-pyrrolidone (NMP) is prepared. The mold is cleaned with ethanol and placed inside a petri dish. Then the solution is poured over the mold and air bubbles are removed by applying a vacuum. The solution is heated to 80 °C until the NMP is evaporated. Deionized water is added to dissolve the remaining NMP and again heated to 80 °C. Finally, the membrane is placed in a vacuum oven to remove all water and NMP. The thickness of the membrane (w) is determined with a micrometer screw gauge and the extrusion height (h) with microscopy images, these are given in Table 3.1. There is a large difference in the membrane thickness between samples. Apparently, the wafer was not completely horizontal inside the petri dish.

Table 3.1 – Membrane parameters corresponding to Figure 3.3. Extrusion height is determined by microscopy images and the thickness of the membrane with a micrometer screw gauge.

L (µm)	**h** (µm)	**w** (µm)
0 (flat)	0	835 ± 67
100	41 ± 10	704 ± 20
200	31 ± 9	427 ± 25
800	42 ± 7	135 ± 19

3.3 Method

The goal of this research is to investigate the effect of topology features on OLC. The main drawback of operating in the OLC regime is the energy penalty due to the plateau region and lower slope of the OLC region. In the plateau region the potential is increased, without gaining significant ion transfer, as discussed in section 2.3. Therefore, the length of the plateau should be as short as possible. A second interesting parameter is the magnitude of OLC. In the end the current density should be as high as possible. To investigate this, electrochemical and FLIM experiments are carried out.

3.3.1 Electrochemical experiments

In electrochemical experiments, the relation between current and potential can be measured. This is an important tool to investigate ion concentration polarization. A potentiostat (Metrohm Autolab PGSTAT204) controls the potential difference between the anode and cathode and measures the current through the sensing electrodes. The anode is connected to the working electrode and becomes positively charged. The cathode is connected to the counter electrode and becomes negatively charged. Copper dissolves from the anode and is deposited on the cathode. Therefore, the cathode is cleaned before every experiment to remove the deposited copper. The membrane is placed between the electrodes with the topology features facing the anode, as this compartment will be depleted. The two compartments are rinsed with deionized water and dried with a tissue. The electrolyte is then added to the compartments and the desired potential is applied.

Current-voltage curve

In order to see the influence of the different structured membranes, an i-V curve will be constructed. A typical i-V curve is shown in Figure 3.4a. The current density is obtained at steady state conditions. In this research, the potential difference is increased from 0.1 V to 2.5 V with steps of 0.1 V. With every increase in potential, the system slightly changes and a new steady state has to be reached. Due to limitations related to the set-up (e.g. deposition of copper, leakages), it is not

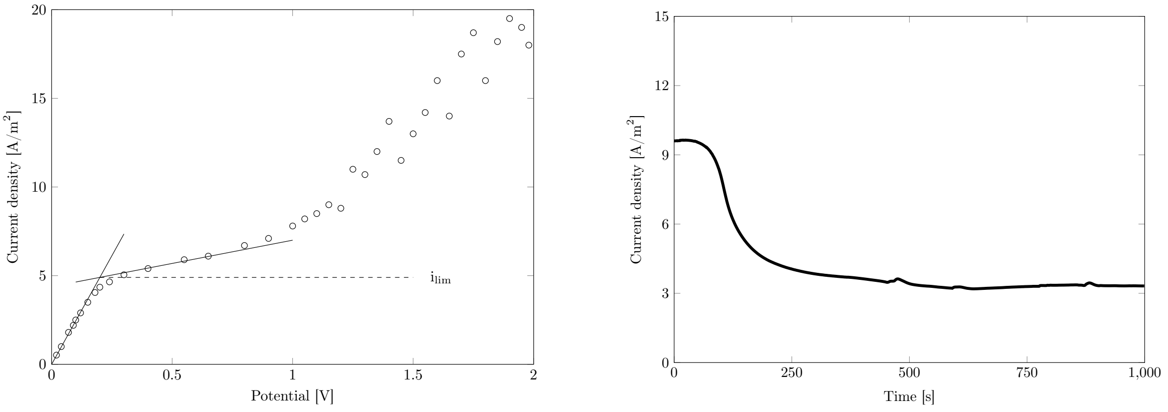

(a) Typical i-V curve.[39]

(b) Typical chronoamperometry curve.

Figure 3.4 – Typical curves obtained by a) i-V measurements and b) chronoamperometry measurements.

possible to reach equilibrium at every potential. The maximum time at each potential is about 50 s. For a larger time step, leakages will disturb the experiment before the sweep is completed. Also copper dendrites will form at long experiments (>1200 s) and high voltages (>2 V).[4]

Chronoamperometry

In chronoamperometry, the current is measured over time with a fixed potential difference between the sensing electrodes. This is useful to (1) determine the steady state current density for a certain potential difference and (2) determine the time until steady state is reached. Both compartments are filled with the electrolyte solution, hence each experiment starts off with a uniform concentration profile. At $t = 0$, the potential difference is applied and kept constant for 1000 s. A typical curve obtained from chronoamperometry is shown in Figure 3.4b.

During the i-V curve experiments, equilibrium will not be reached for each potential after 50 s. Especially in the transition between the Ohmic and plateau region. In this region, CP sets in and a strong decrease in current density is observed. Chronoamperometry experiments are carried out in this region to investigate the real onset of the plateau region.

3.3.2 Fluorescence lifetime imaging microscopy

Fluorescence lifetime imaging microscopy (FLIM) is used to obtain a concentration profile of the diluted department of the electrodialysis cell. This gives additional information on how the system changes when the topology of the membrane is changed. Using FLIM, a concentration profile can be obtained at several moments during the experiment.

The principle of FLIM can be explained using the Jablonski diagram shown in Figure 3.5. A photon is exited from the ground state (S_0) to a state of higher energy (S_1). It rapidly falls down ($< 10^{-12}$ s) to the lowest vibrational level of S_1. Fluorescence is the return of the photon to the ground state. The time between excitation and return is defined as the fluorescence lifetime (τ) and is usually in the order of nanoseconds. In this setup, the fluorescence lifetime data is retrieved via frequency-domain data acquisition. Light is sinusoidally modulated. Between emission and return of the light it undergoes a phase shift and change in amplitude. From this data, two lifetimes can be calculated: the phase lifetime (τ_p) and the modulation lifetime (τ_M). Hence, in frequency-domain data acquisition the lifetime is not directly measured, but calculated. [40–43]

A crucial property of fluorescence lifetime is that it does not depend on the fluorescence intensity and concentration. Internal factors (e.g. molecular rotation) and external factors can influence the lifetime (e.g. the presence of fluorescence quenchers). Therefore it might be possible that the lifetime is influenced by the copper- and/or sulphate ion concentration. Finding a fluorophore that is affected by the system is essential. For the $CuSO_4$ electrolyte system it has been found that the lifetime of Alexa Fluor® 488 changes when altering the electrolyte concentration. A modified Stern-Volmer equation (eq. (3.4)) is used to fit the experimental data, since it was found to describe the data very well.[40] The calibration curve for this system is shown in Figure 3.6.

$$\tau = A\left(1 - \frac{1}{\frac{1}{fKc} + \frac{1}{f}}\right) \tag{3.4}$$

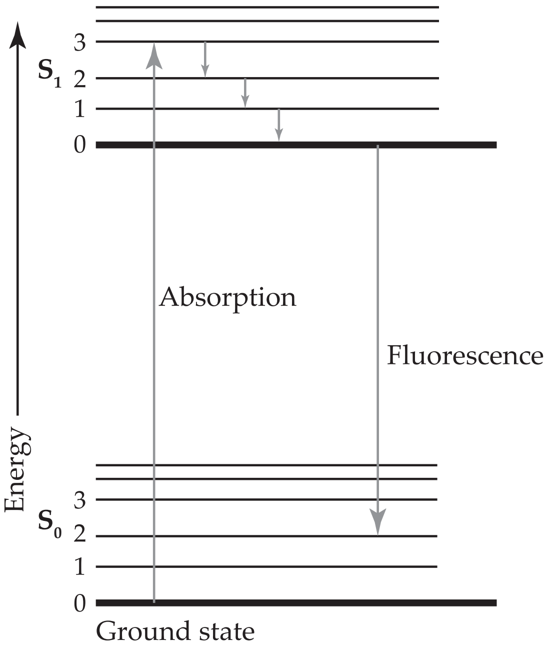

Figure 3.5 – Jablonski diagram of fluorescence.[40]

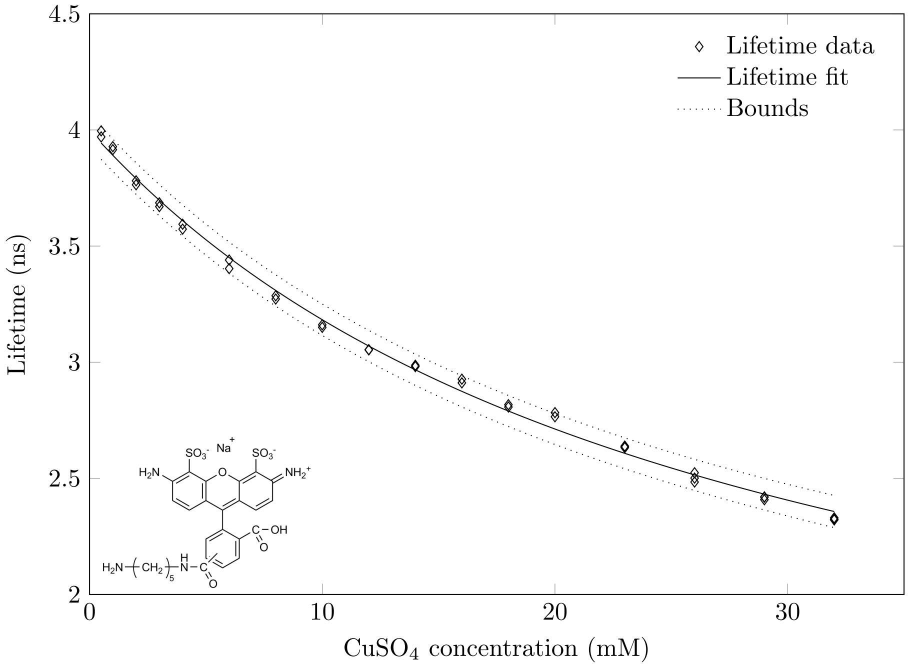

Figure 3.6 – Calibration curve with 95 % confidence intervals (residuals are checked by visual inspectation of the normal probability plot). The data is fitted to a modified Stern-Volmer equation. The best fit is obtained with $A = 4.00 \pm 0.03$, $K = 0.0367 \pm 0.0055$ and $f = 0.760 \pm 0.055$

The same initial electrolyte concentration (10 mM) is used as in the electrochemical experiments. Alexa Fluor® 488 is added to the mixture in a concentration of 2.5 µM or 5 µM. This is a sodium salt; additional charge carriers are therefore added to the system. To ensure the transport of Na^+ ions does not significantly contribute to the total ion transport, the concentration of dye should be negligible compared to the electrolyte concentration. Since lifetime is calculated and not directly measured, a reference sample with a known lifetime is necessary. A reference solution of only dye (2.5 µM or 5 µM) with a known fluorescence lifetime of 4.1 ns is used. From the fit it follows that $\tau(0) = A = 4.00 \pm 0.03$, which is not the same as the reference lifetime. Therefore the fit cannot be extrapolated to very low concentrations of salt.

For each experiment, both compartments of the cell are filled with the mixture of electrolyte and dye. The electrodes are attached and the experiment is started. Using FLIM a lifetime profile is obtained every 25 s. First the FLIM is started and a first lifetime profile will be obtained without an applied potential difference. Then a fixed potential of 1 V is applied for 1000 s. In total, 45 lifetime profiles at different times are obtained. Table 3.2 gives the input parameters for the FLIM experiments. The optimal modulation frequency is determined from the reference lifetime. To magnify the lifetime signal, a microchannel plate (MCP) is used. The rate of magnification can be controlled with the MCP gain.[43] With increasing dye concentration, also the intensity increases. The MCP gain then has to be lowered to avoid overexposure.

Table 3.2 – Parameters for FLIM experiments. The MCP gain is 550 V when using a 2.5 µM dye concentration and 510 V when using a 5 µM dye concentration.

Parameter	**Value**
Reference lifetime	4.1 ns
Modulation frequency	25 MHz
Exposure time	300 ms
Phase	30 °
MCP gain	510 or 550 V

4 | Numerical simulations

4.1 Theoretical framework

To gain more insight in the effect of topology features on overlimiting current (OLC), a set of equations corresponding to the experimental system will be solved numerically. The model will be solved in 2 dimensions and the topology of the membrane can easily be adjusted. Numerically, the system can be described by a Poisson-Nernst-Planck with Navier-Stokes framework. This couples the concentration profile, velocity field and electrical potential distribution.

4.1.1 Governing equations

General mass conservation of a certain species in the system is expressed by Eq. (4.1). A distinction is made between cations (Cu^{2+}) and anions (${SO_4}^{2-}$), other species in the system are neglected. Dimensionless variables are indicated without overline, whereas their dimensionalized counterparts are indicated with overline. The non-dimensionalization follows the approach of Druzgalski and Mani.[44]

$$\frac{\partial \overline{c}^{\pm}}{\partial \overline{t}} = -\overline{\nabla} \cdot \overline{\mathbf{J}}^{\pm} \tag{4.1}$$

Eq. (4.2) gives the Nernst-Planck equation, a detailed derivation can be found in Appendix C. It combines mass transport driven by a concentration gradient (diffusion), a potential gradient (migration) and convective mass transport. This is a simplification of the Maxwell-Stefan equation, assuming an ideal, dilute solution.

$$\overline{\mathbf{J}}^{\pm} = \underbrace{-D\overline{\nabla}\overline{c}^{\pm}}_{\text{Diffusion}} \underbrace{-\frac{zDe}{k_B T}\overline{c}^{\pm}\overline{\nabla}\overline{\phi}}_{\text{Migration}} + \underbrace{\overline{c}^{\pm}\overline{\mathbf{u}}}_{\text{Convection}} \tag{4.2}$$

The electrical potential can be expressed by the Poisson equation. This gives the relationship between the charge density and electrical potential. Here, the relative permittivity is assumed to remain constant while varying the concentration.

$$-\varepsilon_r \varepsilon_0 \overline{\nabla}^2 \phi = ze(\overline{c}^{+} - \overline{c}^{-}) \tag{4.3}$$

The velocity field is solved with the Navier-Stokes equations. With the experimental setup, the Reynolds number is low ($\mathcal{O}(10^{-3})$), therefore the nonlinear inertial term is neglected. Also the influence of buoyancy forces is not taken into account. The orientation of the setup in the Earth's gravity field minimises the effect of gravitational convection.[4] Then the Navier-Stokes equations become:

$$\rho\frac{\partial\overline{\mathbf{u}}}{\partial\overline{t}} = \underbrace{-\overline{\nabla}\overline{p}}_{\text{Pressure}} + \underbrace{\overline{\nabla}\cdot(\mu\overline{\nabla}\overline{\mathbf{u}})}_{\text{Viscosity}} - \underbrace{ze(\overline{c}^{+}-\overline{c}^{-})\overline{\nabla}\overline{\phi}}_{\text{Electric field}} \tag{4.4}$$

$$\overline{\nabla}\cdot\overline{\mathbf{u}} = 0 \tag{4.5}$$

The equations are transformed into a dimensionless form using the following characteristic scales:[44]

$$t_{\text{diff}} = \frac{L^2}{D} \quad , \quad \mathbf{u}_{\text{diff}} = \frac{D}{L} \quad , \quad V_T = \frac{k_B T}{ze} \quad , \quad p_0 = \frac{L^2}{\mu D} \quad , \quad \mathbf{J}_0 = \frac{D c_{rel}}{L} \tag{4.6}$$

$$t = \frac{\overline{t}}{t_{\text{diff}}} \ , \ \mathbf{u} = \frac{\overline{\mathbf{u}}}{\mathbf{u}_{\text{diff}}} \ , \ \phi = \frac{\overline{\phi}}{V_T} \ , \ p = \frac{\overline{p}}{p_0} \ , \ \nabla = \overline{\nabla}L \ , \ c^{\pm} = \frac{\overline{c}^{\pm}}{c_{rel}} \ , \ \mathbf{J} = \frac{\overline{\mathbf{J}}}{\mathbf{J}_0} \tag{4.7}$$

Using the correlations in Eq. (4.7), the governing equations can be rewritten in dimensionless form, Eq. (4.8) - (4.12).[44]

$$\frac{\partial c^{\pm}}{\partial t} = -\nabla\cdot\mathbf{J}^{\pm} \tag{4.8}$$

$$\mathbf{J}^{\pm} = -\nabla c^{\pm} \mp c^{\pm}\nabla\phi + c^{\pm}\mathbf{u} \tag{4.9}$$

$$-2\epsilon^2\nabla^2\phi = c^{+} - c^{-} \tag{4.10}$$

$$\frac{1}{\text{Sc}}\frac{\partial\mathbf{u}}{\partial t} = -\nabla p + \nabla^2\mathbf{u} - \frac{\kappa}{2\epsilon^2}(c^{+}-c^{-})\nabla\phi \tag{4.11}$$

$$\nabla\cdot\mathbf{u} = 0 \tag{4.12}$$

This introduces three dimensionless numbers; the Schmidt number ($\text{Sc} = {}^{\mu}/_{\rho D}$) is the ratio between momentum diffusivity and mass diffusivity.[45] In this system it is $\mathcal{O}(10^3)$. The second number is the dimensionless electrical double layer (EDL) size (ϵ), which scales the Debye length to the characteristic length scale of the system.[44]

$$\epsilon = \frac{\lambda_D}{L} \quad , \quad \lambda_D = \sqrt{\frac{\varepsilon_r\varepsilon_0 k_B T}{2(ze)^2 c_{rel}}} \tag{4.13}$$

The last dimensionless number is the electrohydrodynamic coupling constant, κ, defined as:

$$\kappa = \frac{\varepsilon_r\varepsilon_0}{\mu D}\left(\frac{k_B T}{ze}\right)^2 \tag{4.14}$$

4.1.2 Boundary conditions

The domain is enclosed by two cation-selective surfaces, the anode and the membrane, and two impermeable walls. Figure 4.1 shows the representation of the system, with a 800 µm structured membrane, used in the simulations including the the boundary conditions. At the membrane surface ($y = 0$) there is a no slip and a no flux condition assumed for the fluid. For the cations there is a fixed concentration and the anions have a no flux condition. The electric potential is grounded at the membrane. At the anode ($y = 2$), the fluid is not able to go through and no slip is assumed. It also is a cation-selective interface and therefore impermeable for anions. The electric potential is set at a certain value and the cation concentration is set at $2c_0$. This is obtained from literature [44] and fluorescence lifetime imaging microscopy experiments.[4] Two impermeable walls close the system. A no-slip condition is applied here for the fluid velocity. Only half of the cell will be simulated, that means one of the walls will have a symmetry condition. At $t = 0$, the fluid is not moving and the concentration is uniform with $c^{\pm} = c_0$. The electrical potential at $t = 0$ is 0 in the whole system.

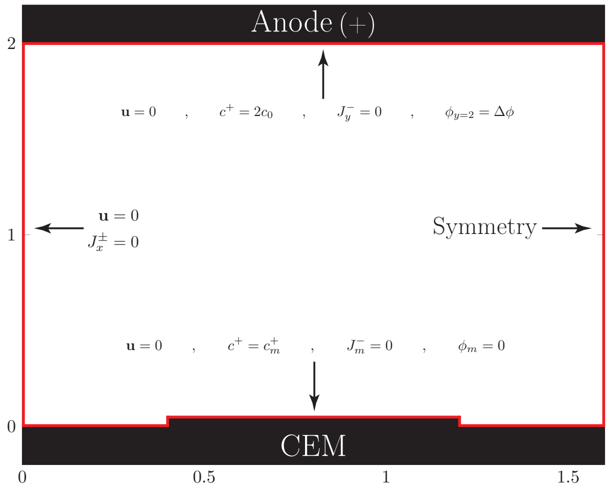

Figure 4.1 – Representation of the system as it is used in the simulations. The conditions at each boundary are included. This is for a 800 µm structured membrane.

4.1.3 Assumptions

The chosen governing equations and boundary conditions indicate certain assumptions. Important assumptions are listed below.

- the mixture acts like an ideal system (activity coefficient = 1),
- there are only water-ion frictions,
- the water fraction is 1, an infinitely dilute system is assumed,
- Cu^{2+} and $SO_4{}^{2-}$ are the only two species present in the system,
- the non-linear inertial term can be neglected,
- the influence of gravitational convection can be neglected,
- the relative permittivity is constant and not a function of concentration,
- only cations are able to permeate the membrane,
- a no slip condition for the fluid is assumed at the boundaries,
- a certain fix concentration (zeta potential) is assumed at the membrane.

4.2 Input parameters

Input parameters are given in Table 4.1. The Debye length for this system is ~50 nm, which gives a dimensionless EDL size (ϵ) of $\mathcal{O}(10^{-5})$. It will take a large degree of computational power to resolve the EDL at this length scale. It has been shown previously that ion transport is not very sensitive to changes in ϵ.[44, 46] Therefore the value of ϵ is set at 10^{-3}. This seems to be a reasonable trade off between the scale of the EDL and the computational cost.[44, 46] κ and Sc are calculated from the physical properties of the system. The desired potential difference over the whole system is 1 V, that is between the sensing electrodes. In the simulations only the part between membrane and anode is considered. The potential difference over this system is not known and also might not be constant over time due to changes in resistance. For the simulations it is assumed to be 0.5 V, which corresponds to 39.8 V_T. The concentration is scaled against the initial concentration of 10 mM. The dimensionless cation concentration at the membrane surface is set at 2, which has been used in previous simulations of similar systems.[44, 46]

Table 4.1 – Dimensionless input parameters for the numerical model.

Parameter	**Value**	**Description**
ϵ	10^{-3}	Electrical double layer size
κ	0.13	Electrohydrodynamic coupling constant
Sc	1170	Schmidt number
$\Delta\phi$	39.8	Applied voltage
c_0	1	Initial concentration
c_m^+	2	Cation concentration at the membrane surface

This numerical framework is solved via the finite element method in COMSOL Multiphysics 5.2. The potential and concentration profiles are solved using quadaratic Lagrangian elements and the Stokes equation is solved with P2-P1, second order elements for velocity and first order elements for pressure. A refined mesh near the membrane and anode surface is used to achieve mesh independence. The system is solved time-dependent up to a dimensionless time of 2, corresponding to ~2350 s, to make sure the system reaches steady-state conditions

5 | Results and discussion

5.1 Current-voltage characterization

An i-V can show the effect of membrane structures on ion transport. i-V curves show the transition between the Ohmic region and plateau region and between the plateau region and overlimiting current (OLC) region. Figure 5.1a shows a typical i-t curve when following the experimental plan described in section 3.3. The potential is increased from 0.1 V to 2.5 V with steps of 0.1 V. The final value at each potential ($\tau = 50\,\mathrm{s}$) is taken as the measured current density at that potential. A longer duration of one experiment was not possible due to leakages and subsequent bubble formation. For the final i-V curve, the average of multiple runs is calculated, including the standard deviation, resulting in a curve as shown in Figure 5.1b.

The i-V curves of all the tested membranes are given in Figure 5.2. Around the start of the plateau region there is an overshoot in current density. Here, the system is not in equilibrium after 50 s. Additional chronoamperometry measurements are carried out in this region and the steady-state current density is determined. Now the plateau length can be determined using the method shown in Figure 5.3. For each region of the i-V curve, the slope is determined. The slopes for the Ohmic and plateau region intersect at the limiting current density (the theoretical value is $2.95\,\mathrm{A/m^2}$). Overlimiting current sets in at the intersect of the slopes of the plateau and OLC region. In Table 5.1 the results are summarised for all membranes, Appendix D gives a more detailed derivation.

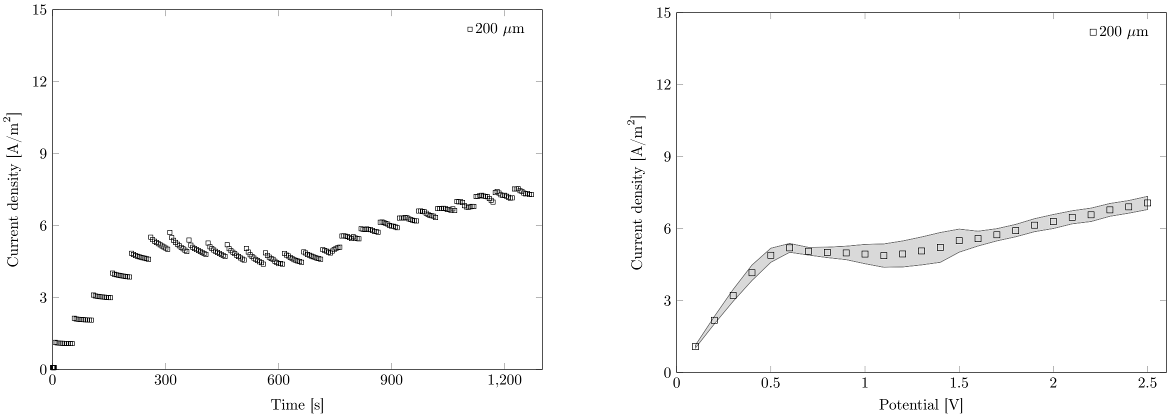

(a) i-t curve

(b) i-V curve

Figure 5.1 – i-t curve data (a) for a 200 µm structured membrane is converted to an i-V curve (b). The final value at each potential is taken as current density. The i-V curve shows the average of at least three measurements with the standard deviation.

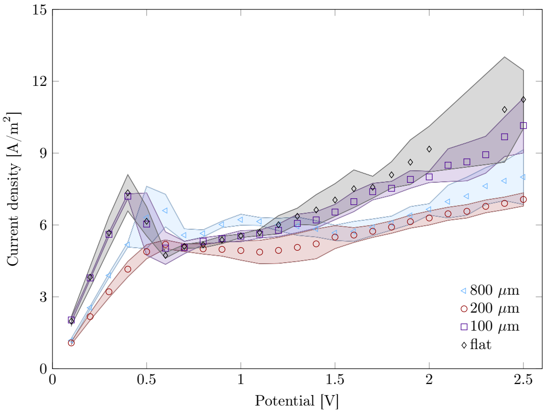

Figure 5.2 – i-V curves of different structured membranes. Data points are the average of multiple experimental runs, the shaded regions represent the standard deviation.

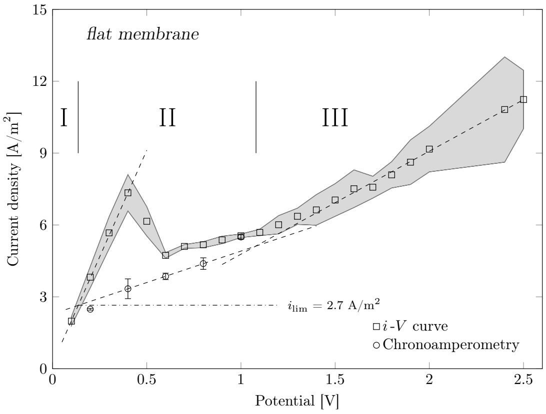

Figure 5.3 – Determination of plateau length for the flat membrane. The Ohmic (I), plateau (II) and OLC (III) region are determined by the intersects of the slopes of the regions.

The membrane thickness differs between the membranes. This will have an influence on the electrochemical response. The distance over which the potential is applied is fixed in all measurements. An increase in membrane thickness will therefore result in a decrease in distance between the membrane and the sensing electrode on the anode side of the membrane. The membrane has a relatively high conductivity, hence the potential difference at the depleted side of the membrane increases. This could result in a higher current density for thicker membranes. Table 5.1 shows the parameters for every membrane, giving the highest slopes for the thickest membranes.

From Figure 5.2 and Table 5.1 there is no clear trend visible regarding the structure size. The system seems highly sensitive to other parameters such as the thickness and curvature of the membrane. Additional experiments using similar membranes with the same thickness are necessary to properly investigate the influence of membrane structures as will be discussed in the recommendations section.

5.2 Chronoamperometry

Chronoamperometric measurements are used to investigate the onset of the plateau region. It gives the steady-state current density at an applied potential of 0.4 V to 1 V. With this, the effect of membrane structures on the magnitude of the plateau can be investigated. Also experimental data are compared with a 2D numerical model of the system. Flow profiles obtained from

Table 5.1 – The plateau length, limiting current density and slopes of the three regions of the i-V curve. The method to determine this is described in Appendix D.

Membrane	**Membrane thickness [µm]**	**Plateau length [V]**	i_{lim} [A/m^2]	**Slope** [S/m^2]		
				Ohmic	***Plateau***	***OLC***
flat	835 ± 67	0.94	2.7	17.8	2.6	4.3
100 µm	704 ± 20	0.70	3.1	17.9	1.7	3.4
200 µm	427 ± 25	0.65	2.4	10.7	1.3	2.4
800 µm	135 ± 19	1.18	4.0	13.3	1.0	2.9

simulations are used to investigate the effect of the extrusion length. Finally, the effect of the curvature of the membrane is investigated numerically. In practice, the membranes tend to bend when placed inside the cell (as can be seen from the FLIM images in Appendix G). This has an influence on the distribution of the electric field and therefore might significantly influence the results.

The chronoamperometry data (Appendix E) does not show any significant influence of membrane structure on the magnitude of the plateau region. Only at potentials higher than >0.6 V, the flat membrane and 800 µm structured membrane have a higher current density than the 200 µm structured membrane. This is in contrast to previous research were it was concluded that the introduction of these kind of structure on the membrane is beneficial for ion transport.[4] The sensitivity of the experimental system to differences in e.g. membrane thickness and curvature of the membrane makes it difficult to compare these results.

Table 5.2 gives the fluxes from numerical simulations with an electrical potential difference of 0.5V between the anode and membrane. These results show a decrease in ion flux for membranes with intermediate structure sizes. Structures are implemented to enhance the formation of electroconvective vortices. The velocity profiles (Figure 5.4 and Appendix F) show the formation of these vortices, also for a flat membrane. When a structure is present, the vortices tend to be located on the edges of the extrusion. Which indicates that the size of the vortices is proportional to the extrusion length. It is beneficial for mass transport enhancement to mix as much of the diffusion layer as possible. In this system the diffusion layer of membrane and anode overlap, therefore large vortices are desired. For the 100 µm structured membrane, the extrusions are too small for the vortices to be formed at the extrusion edges. There are only large vortices, disturbed by the surface, decreasing the ion flux a little compared to the flat membrane.

The magnitude of the current density is lower than measured experimentally. Parameters such as applied potential, concentration at the membrane and EDL size are estimated and can be used to fit the model to the experimental data. The trend in the numerical data is similar as the trend in the experimental results (400 µm is not measured experimentally). Also in the simulations the flat and 800 µm structured membranes have the highest flux. This indicates that the implementation of structures on the surface of the membrane is only beneficial above a certain structure size. In this system the threshold structure size seems to be around 800 µm.

During the experiments, the membranes tend to bend when placed inside the cell. As a result, the electric field lines are curved which most likely influences the formation of electroconvective vortices. Numerical simulations have been carried out for membranes with a curved surface without structures. This has shown to increase the ion flux through the membrane with 10 % to 30 %. This shows the need for additional experiments with membranes of the same thickness which at least have the same curvature, but preferably do not bend at all.

Table 5.2 – The current density for multiple structured membranes obtained from numerical simulations. A potential difference of 0.5 V is applied between the anode and the membrane.

	Current density [A/m^2]
flat	3.47
100 µm	3.39
200 µm	2.62
400 µm	2.72
800 µm	3.57

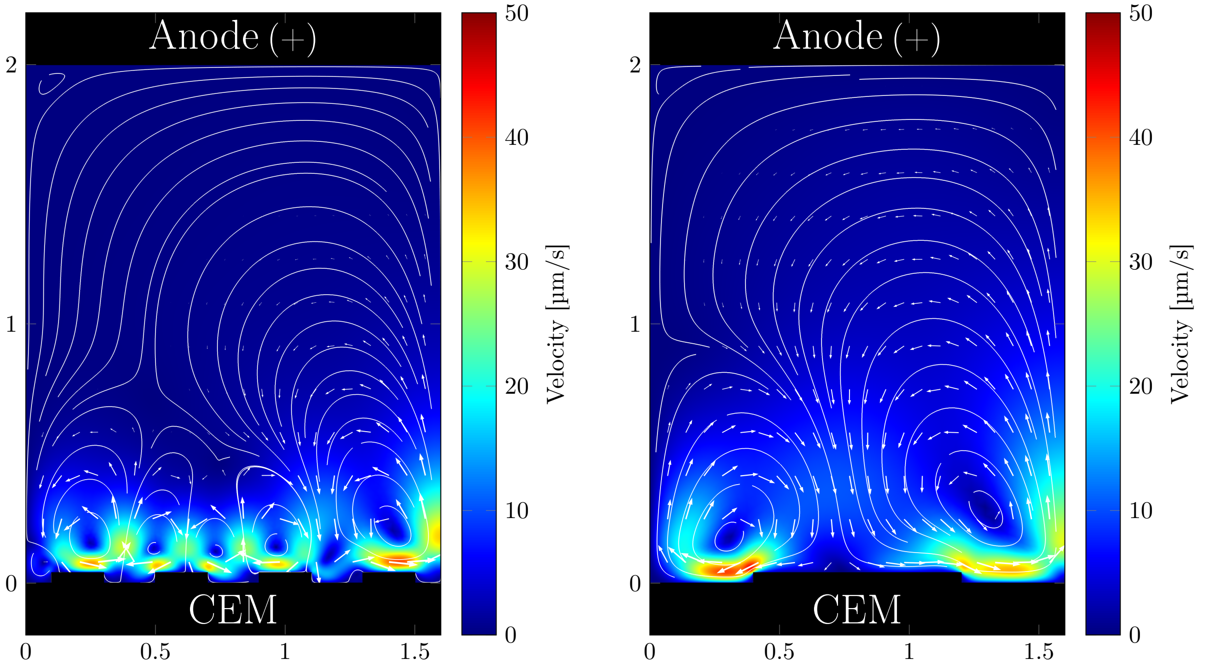

(a) Velocity profile for a 200 µm structured membrane.

(b) Velocity profile for an 800 µm structured membrane..

Figure 5.4 – Velocity profiles for a 200 µm and an 800 µm structured membrane obtained from numerical simulations. Vortices are located at the edges of the extrusions.

5.3 Ohmic region

The shape of the chronoamperometric curves are all very similar; in the first seconds there is a constant current density. Then the compartment gets depleted of ions and diffusion limitations set in. Finally, a steady-state current density is achieved. At 0.4 V however, this does not hold for the structured membranes, only for the flat membrane (Figure 5.5). Membranes with a structure have a more linear decay until a steady-state is reached, meaning there is no sudden drop in current density over time before a new steady-state is reached at 0.4 V. At an higher potential this does not occur, therefore it may be a phenomenon only occurring in the Ohmic region.

To investigate this, additional experiments at 0.2 V were carried out. The results are shown in Figure 5.6. At this potential there is almost no decay in current density at all. This small decay can be attributed to the increasing resistance of the system due to e.g. copper deposition. Experiments at 0.2 V (Ohmic region) show this smooth linear decay for all membranes and experiments at $\geq$ 0.6 V (plateau/OLC region) show a sudden drop in current density. This indicates the smooth decay is characteristic for the Ohmic region, whereas the drop in current density is characteristic for the plateau and OLC region. The flat membrane is then at 0.4 V already in the plateau region, whereas the structured membrane is still in the Ohmic region, hence, extends the working range of the structured membrane in the Ohmic region. This can be interesting since most electrochemical processes are operated just below the limiting current density. Chronoamperometric experiments with an applied potential of 0.3 to 0.6 V will give more insight on this phenomenon.

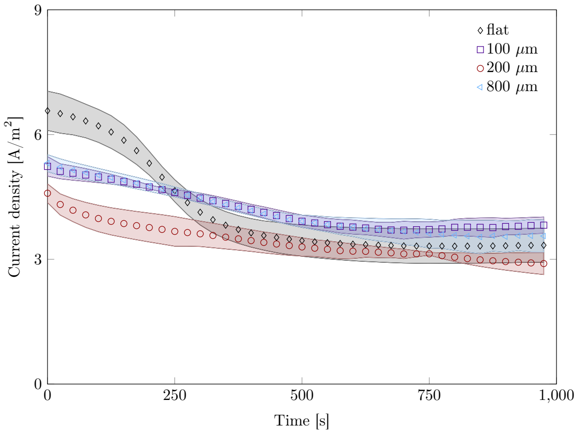

Figure 5.5 – Chronoamperometry experiments at 0.4 V showing a different decay in current density for the flat membrane compared to the structured membranes.

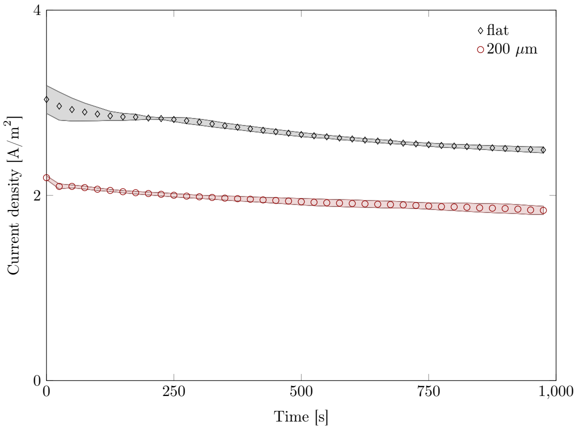

Figure 5.6 – Chronoamperometry experiments at 0.2 V for a flat membrane and 200 µm structured membrane showing only little decay in current density over time.

5.4 Equilibrium time

The time until equilibrium is reached is a measure for how quickly a system adjust to changes in operating conditions. In this section the influence of membrane structure size and applied potential are investigated.

Table 5.3 gives the time until equilibrium is reached for the measured potentials and membranes. The equilibrium current density (i_{eq}) is chosen as the final data point of the chronoamperometry curves. For these calculations, it is assumed that equilibrium is reached when $i/i_{eq} = 1.1$. The time until equilibrium is reached is about 300 s to 400 s, except for a 200 µm structured membrane and for a potential of 1 V. For the 200 µm structured membrane it takes longer until equilibrium. The lower slope of the curve results in larger confidence intervals. When a potential of 1 V is applied, there are larger differences between the individual experiments at the same conditions. Also oscillations in current density occur near the end of the experiment and it is difficult to obtain the equilibrium current density. This results in large error margins and deviating equilibrium times.

A 1D numerical model has been made to predict the concentration decay over time in the Ohmic region. This can be used instead of the 2D model, since electroconvection is not dominant in this region and it will drastically decrease the simulation time. So far, no results comparable to experimental data has been obtained. Finding the most suitable boundary conditions should be the first attempt to improve the model. Secondly, the effect of electro-osmosis should be investigated, since fluid velocity effects are not taken into account.

Table 5.3 – The time in seconds until equilibrium is reached is given for all tested membranes and potentials. Here, the point were $i = 1.1i_{eq}$ is taken as equilibrium time.

Membrane	**0.4V**	**0.6V**	**0.8V**	**1V**
flat	389 ± 74	399 ± 78	397 ± 51	626 ± 401
100 µm	391 ± 58	361 ± 99	381 ± 52	340 ± 488
200 µm	646 ± 245	451 ± 151	615 ± 74	500 ± 104
800 µm	478 ± 212	313 ± 105	283 ± 60	274 ± 70

5.5 Concentration profiles

Fluorescence lifetime imaging microscopy (FLIM) is used to visualize concentration profiles. A fluorescent dye is added to the electrolyte solution and the lifetime is measured. Every 25 s a fluorescence lifetime profile is obtained and this can be converted to a concentration profile using the calibration curve in Figure 3.6. The profiles are obtained for chronoamperometry measurements at 1 V.

Figure 5.7 shows concentration profiles obtained by FLIM images at $t = 0$ s and $t = 900$ s for an 800 µm structured membrane. At the start of the experiment there is a uniform concentration profile (Figure 5.7a). Over time, concentration polarization sets in and ions are depleted at the membrane surface (Figure 5.7b).

The measured lifetime is not a function of fluorophore concentration or intensity. However, a certain concentration of dye is required in order to obtain a lifetime signal. In Figure 5.8a, the structures of the 200 µm structured membrane are not clearly visible. The dye is not retained between the structures. The fluorophore, Alexa Fluor® 488, is negatively charged and becomes depleted from the membrane interface resulting in Figure 5.8b. The membrane is not visible due to the absence of dye close to the membrane. Increasing the dye concentration by a factor two did not improve the measurements.

At multiple points in time, concentration profiles perpendicular and parallel to the membrane are obtained. Figure 5.9 shows the concentration profiles for a 800 µm structured membrane. The data are averaged over 20 pixels and smoothened to obtain the curves. Error margins are obtained for each data point from the FLIM calibration curve. When averaging the data, also the errors are averaged. At $t = 0$ s, there is a uniform concentration profile. It develops to a linear profile, but it seems to flatten near the membrane surface. This indicates the formation of vortices between the diffusion layer and membrane surface. Figure 5.9b shows the profile at 150 µm from the membrane, were the solution gets depleted over time. The concentration decreases over time, but remains constant in x-direction.

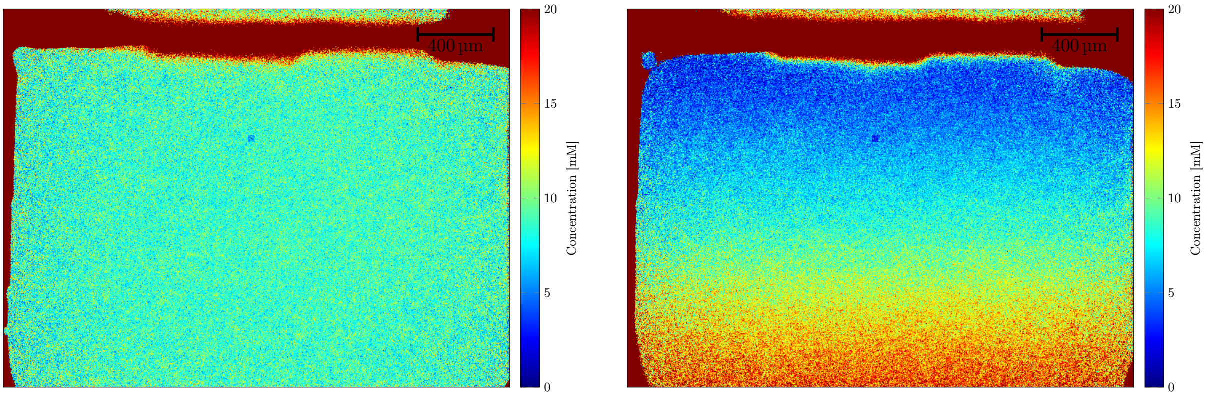

(a) Concentration profile at $t = 0$ s

(b) Concentration profile at $t = 900$ s

Figure 5.7 – Concentration profiles obtained by FLIM images at (a) $t = 0$ s and (b) $t = 900$ s for a 800 µm structured membrane.

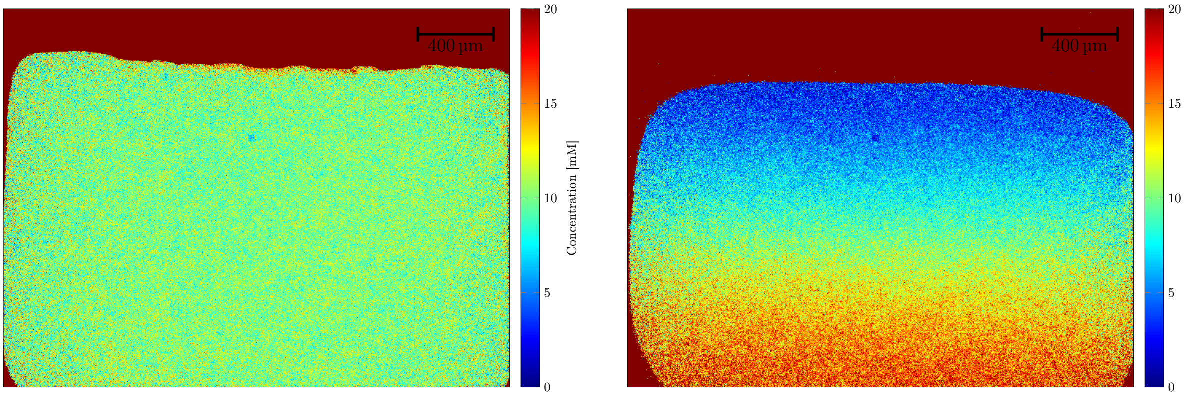

(a) Concentration profile at $t = 0\,\mathrm{s}$

(b) Concentration profile at $t = 900\,\mathrm{s}$

Figure 5.8 – Concentration profiles obtained by FLIM images at (a) $t = 0\,\mathrm{s}$ and (b) $t = 900\,\mathrm{s}$ for a 200 µm structured membrane. In (b) the dye concentration on near the membrane gets depleted and there is no lifetime measured.

Concentration profiles are obtained from 2D numerical simulations. In Figure 5.9, experimental and numerical concentration profiles at steady-state ($t = 2350\,\mathrm{s}$) are compared. For the concentration profile perpendicular to the membrane (Figure 5.9), the numerical simulations only deviate from experimental results close to the membrane surface and near the anode. The boundary conditions for concentration are now estimated, but these can be used as fitting parameters. The profile parallel to the membrane (Figure 5.9b) are constant in x-direction. Numerical simulations at steady-state conditions show a different shape and magnitude. These profiles are close to the membrane and it was already shown that in this region the numerical simulations give a lower concentration than observed experimentally. In the simulations, the concentration increases above the extrusion and decreases above the gap. This corresponds to respectively an inflow and outflow of fluid, hence vortices.

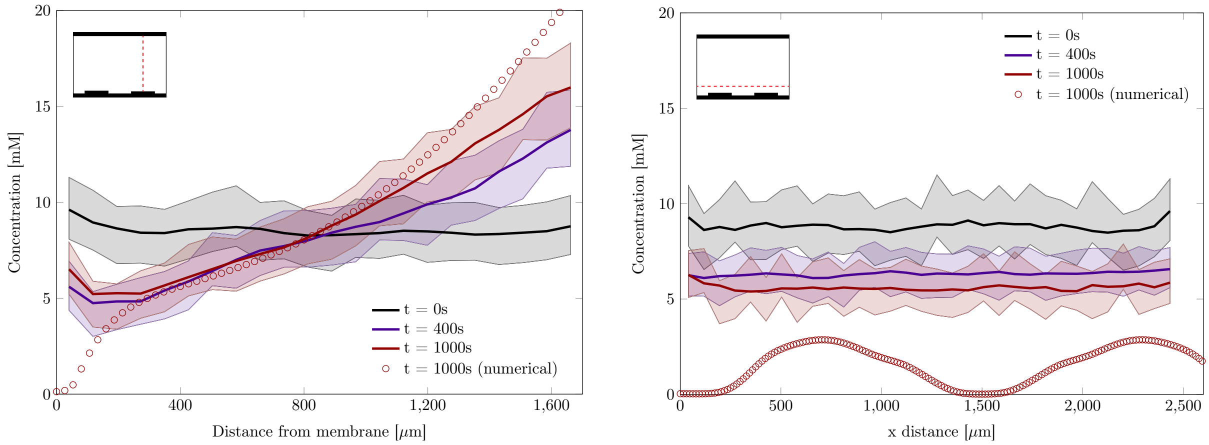

(a) Concentration profiles perpendicular to the membrane at different times. $x = 0$ is at the membrane surface on one of the extrusions.

(b) Concentration profiles parallel to the membrane at a distance of 150 µm from the the membrane surface.

Figure 5.9 – Concentration profiles obtained from FLIM at different points in time perpendicular (a) and parallel (b) to the membrane for a potential of 1 V. Numerical results are included at steady-state conditions for a potential difference of 0.5 V between anode and membrane.

6 | Conclusions and recommendations

The influence of membrane topology features on the electrokinetic and electrohydrodynamic behaviour is experimentally and numerically investigated. Electrical characterization of the system is combined with fluorescence lifetime imaging microscopy (FLIM) to quantify concentration gradients within the system. Numerical simulations of a 2D representation of the system are carried out to interpret the experimental results and potentially extend the research to more complex membrane topology features.

In this research, it is found that structured membranes can have a positive effect on the ion transport properties of an electrodialysis system, as they induces microvortices adjecent to the membrane surface. Depending on the size of the structure this effect is more pronounced. Quantification of local ion concentration shows a linear concentration profile perpendicular to the membrane, which flattens out at the membrane interface, indicating micromixing of this fluid layer.

Chronoamperometric measurements are carried out between 0.2 V and 1 V. This shows the lowest ion flux for a 200 µm structured membrane in the range of 0.6 V to 1 V and comparable fluxes for a flat membrane and 800 µm and 100 µm structured membranes. The same trend in ion flux is obtained from numerical simulations of a 2D representation of the experimental system for a potential difference of 0.5 V between anode and membrane. Velocity profiles (numerical) show the formation vortices on the edges of the extrusions with a vortex size proportional to the extrusion length. Since large vortices are desired to obtain better mixing of the boundary layer, this indicates that the introduction of extrusions on the membrane surface is only beneficial above a certain structure size. Due to the sensitivity of the system to the membrane thickness, additional experiments without differences in membrane thickness are necessary to be able to formulate any firm conclusions.

Experiments at 0.4 V show a more smooth decay for structured membranes compared to the sudden drop in current density observed in experiments with a flat membrane (Figure 5.5). Comparing this decay with experiments at 0.2 V and 0.6 V indicates an earlier onset of the plateau region for flat membranes. Hence, the working range in the Ohmic region is extended by the implementation of structures on the membrane surface. Future research with a potential difference of 0.3 to 0.6 V will give more insight in this phenomenon.

FLIM images have been used to obtain concentration profiles at different points in time. The transformation from a uniform profile at $t = 0\,\mathrm{s}$ to a diffusion layer was observed. Concentration profiles of an 800 µm structured membrane at different points in time are determined. This shows a linear concentration profile, which flattens near the membrane surface. Such a flat concentration profile near the membrane indicates the formation of electroconvective vortices. Parallel to the membrane, a uniform concentration profile is obtained. Close to the membrane, the concentration decreases over time, which corresponds to the depletion of ions near the ion-exchange membrane due to ion concentration polarization. A drawback of Alexa Fluor® 488 as fluorophore is that it will get depleted from the membrane surface. Therefore, a lifetime signal might not be recorded in these regions (Figure 5.8).

From the i-V curves (Figure 5.2) no clear influence of membrane structure size can be distinguished regarding the plateau length or limiting current density. In terms of ion flux, the flat membrane and 100 µm structured membrane seem to have a higher current density in the Ohmic and OLC regions. The difference in membrane thickness and therefore distance between membrane and electrode are expected to have a significant effect on the results. Future experiments constructing an i-V curve should be carried out with membranes of the same thickness. Also improvements of the experimental setup are desired to extend the duration of each experiment.

A 2D numerical representation of the system has been made to compare with experimental results. At steady-state conditions, the trend found in the simulations corresponds to our experimental results. however, the magnitude of ion flux and the time-dependant solutions are different. Optimization of the model can be done by finding suitable boundary conditions for the concentration and the potential difference. The same optimization holds for the 1D model, where attempts to predict the current density decay over time for the Ohmic region were not successful. When the simulations corresponds sufficiently to experimental results, it can be used to find the optimal membrane surface topology. Testing of these 'optimal' membranes (assuming it is possible to synthesize it) in the experimental setup would be the next step in finding the optimal membrane surface topology for electrodialysis processes.

Experiments are carried out in the experimental setup shown in Figure 3.1. This setup gives the possibility to investigate the electrokinetic and electrohydrodynamic behaviour of the system using a variety of techniques, e.g. electrochemical measurements to measure the electrical response, FLIM to obtain concentration profiles and particle image velocimetry to extract the fluid velocity. However, the design of the setup results in some experimental limitations. Leakages occur often and the presence of bubbles is highly disturbing the measurements. This also limits the duration of each experiments, whereas a longer time would make it more easy to construct the i-V curves. Leakages occur mostly on the interface between the cell parts. This is tightened with some screws, but lacks airtight sealing of an O-ring. Membranes have to be cut into the correct shape in order to place it in the cell, which could be improved by using a suitable mold. A membrane which is slightly too large will make it more difficult to tighten the cell parts and has to be compressed resulting in bending of the membrane. When the membrane is too small it will not cover the channel properly and fluids can flow around, yielding a short-cut for ion transport.

The implementation of structures on the membrane surface has an influence on the electrochemical response. Above a certain structure size it seems to increase the ion flux. Also the use of structures on the membrane surface might extend the working range in the Ohmic region. To be able to obtain definitive conclusions and increase the knowledge of the influence of membrane topology features in ion-exchange systems the following future research should be carried out:

- synthesis of structured membranes with the same membrane thickness,
- construction of the i-V curve using i-V sweeps and chronoamperometry experiments with these membranes,
- chronoamperometry measurements between 0.3 V and 0.6 V to investigate the Ohmic region,
- improving the 2D numerical model to find the optimal membrane topology,
- modifications of the experimental setup and
- adjusting the 1D model to predict the current density over time in the Ohmic region.

Bibliography

[1] H. Strathmann, A. Grabowski, and G. Eigenberger. “Ion-exchange membranes in the chemical process industry”. In: *Industrial and Engineering Chemistry Research* 52.31 (2013), pp. 10364–10379. DOI: `10.1021/ie4002102`.

[2] V. V. Nikonenko et al. “Desalination at overlimiting currents: State-of-the-art and perspectives”. In: *Desalination* 342 (2014), pp. 85–106. DOI: `10.1016/j.desal.2014.01.008`.

[3] J. Balster et al. “Morphology and microtopology of cation-exchange polymers and the origin of the overlimiting current”. In: *Journal of Physical Chemistry B* 111.9 (2007), pp. 2152–2165. DOI: `10.1021/jp068474t`.

[4] J. C. De Valença. “Overlimiting current properties at ion exchange membranes”. Thesis. University of Twente, 2017. DOI: `10.3990/1.97890.6543149`.

[5] H. Strathmann. “Membrane Separation Processes, 1. Principles”. In: *Ullmann’s Encyclopedia of Industrial Chemistry*. Wiley-VCH Verlag GmbH & Co. KGaA, 2000. ISBN: 9783527306732. DOI: `10.1002/14356007.a16_187.pub3`.

[6] H. Strathmann. “Electrodialysis, a mature technology with a multitude of new applications”. In: *Desalination* 264.3 (2010), pp. 268–288. DOI: `10.1016/j.desal.2010.04.069`.

[7] H. Jaroszek and P. Dydo. “Ion-exchange membranes in chemical synthesis-a review”. In: *Open Chemistry* 14.1 (2016), pp. 1–19. DOI: `10.1515/chem-2016-0002`.

[8] R. W. Baker. “Membrane Technology”. In: *Kirk-Othmer Encyclopedia of Chemical Technology*. John Wiley & Sons, Inc., 2000. ISBN: 9780471238966. DOI: `10.1002/0471238961.1305130202011105.a01.pub2`.

[9] A. Grabowski et al. “Production of high-purity water by continuous electrodeionization with bipolar membranes: Influence of concentrate and protection compartment”. In: *Separation and Purification Technology* 60.1 (2008), pp. 86–95. DOI: `10.1016/j.seppur.2007.07.052`.

[10] R. E. Lacey. “Energy by reverse electrodialysis”. In: *Ocean Engineering* 7.1 (1980), pp. 1–47. DOI: `10.1016/0029-8018(80)90030-X`.

[11] K. Nagasubramanian, F. P. Chlanda, and K. J. Liu. “Use of bipolar membranes for generation of acid and base - an engineering and economic analysis”. In: *Journal of Membrane Science* 2.C (1977), pp. 109–124. DOI: `10.1016/S0376-7388(00)83237-8`.

[12] Y. Mizutani. “Structure of ion exchange membranes”. In: *Journal of Membrane Science* 49.2 (1990), pp. 121–144. DOI: `10.1016/S0376-7388(00)80784-X`.

[13] R. K. Nagarale, G. S. Gohil, and V. K. Shahi. “Recent developments on ion-exchange membranes and electro-membrane processes”. In: *Advances in Colloid and Interface Science* 119.2-3 (2006), pp. 97–130. DOI: `10.1016/j.cis.2005.09.005`.

[14] H. Strathmann. “Membrane Separation Processes, 4. Concentration Polarization and Membrane Fouling”. In: *Ullmann’s Encyclopedia of Industrial Chemistry*. Wiley-VCH Verlag GmbH & Co. KGaA, 2000. ISBN: 9783527306732. DOI: `10.1002/14356007.o16_o05`.

[15] E. V. Dydek and M. Z. Bazant. "Nonlinear dynamics of ion concentration polarization in porous media: The leaky membrane model". In: *AIChE Journal* 59.9 (2013), pp. 3539–3555. DOI: `10.1002/aic.14200`.

[16] J. J. Krol, M. Wessling, and H. Strathmann. "Concentration polarization with monopolar ion exchange membranes: Current-voltage curves and water dissociation". In: *Journal of Membrane Science* 162.1-2 (1999), pp. 145–154. DOI: `10.1016/S0376-7388(99)00133-7`.

[17] V. V. Nikonenko et al. "Intensive current transfer in membrane systems: Modelling, mechanisms and application in electrodialysis". In: *Advances in Colloid and Interface Science* 160.1-2 (2010), pp. 101–123. DOI: `10.1016/j.cis.2010.08.001`.

[18] J. H. Choi, H. J. Lee, and S. H. Moon. "Effects of electrolytes on the transport phenomena in a cation-exchange membrane". In: *Journal of Colloid and Interface Science* 238.1 (2001), pp. 188–195. DOI: `10.1006/jcis.2001.7510`.

[19] R. Simons. "The origin and elimination of water splitting in ion exchange membranes during water demineralisation by electrodialysis". In: *Desalination* 28.1 (1979), pp. 41–42. DOI: `10.1016/S0011-9164(00)88125-4`.

[20] Y. Tanaka. "Water dissociation in ion-exchange membrane electrodialysis". In: *Journal of Membrane Science* 203.1-2 (2002), pp. 227–244. DOI: `10.1016/S0376-7388(02)00011-X`.

[21] V. I. Zabolotsky, V. V. Nikonenko, and N. D. Pismenskaya. "On the role of gravitational convection in the transfer enhancement of salt ions in the course of dilute solution electrodialysis". In: *Journal of Membrane Science* 119.2 (1996), pp. 171–181. DOI: `10.1016/0376-7388(96)00121-4`.

[22] T. S. Sorensen. *Surface chemistry and electrochemistry of membranes*. Vol. 79. Surfactant science Series. New York: Marcel Dekker, Inc, 1999. ISBN: 0-8247-1922-0.

[23] G.T. Barnes and I.R. Gentle. *Interfacial Science: An Introduction*. 2nd ed. New York: Oxford University Press Inc., 2011. ISBN: 978-0-19-957118-5.

[24] S. S. Dukhin. "Electrokinetic phenomena of the second kind and their applications". In: *Advances in Colloid and Interface Science* 35.C (1991), pp. 173–196. DOI: `10.1016/0001-8686(91)80022-C`.

[25] N. A. Mishchuk and P. V. Takhistov. "Electroosmosis of the second kind". In: *Colloids and Surfaces A: Physicochemical and Engineering Aspects* 95.2-3 (1995), pp. 119–131. DOI: `10.1016/0927-7757(94)02988-5`.

[26] T. Pundik, I. Rubinstein, and B. Zaltzman. "Bulk electroconvection in electrolyte". In: *Physical Review E - Statistical, Nonlinear, and Soft Matter Physics* 72.6 (2005). DOI: `10.1103/PhysRevE.72.061502`.

[27] B. D. Storey, B. Zaltzman, and I. Rubinstein. "Bulk electroconvective instability at high Péclet numbers". In: *Physical Review E - Statistical, Nonlinear, and Soft Matter Physics* 76.4 (2007). DOI: `10.1103/PhysRevE.76.041501`.

[28] S. M. Davidson, M. Wessling, and A. Mani. "On the Dynamical Regimes of Pattern-Accelerated Electroconvection". In: *Scientific Reports* 6 (2016), p. 22505. DOI: `10.1038/srep22505`.

[29] J. C. De Valença et al. "Dynamics of microvortices induced by ion concentration polarization". In: *Physical Review E - Statistical, Nonlinear, and Soft Matter Physics* 92.3 (2015). DOI: `10.1103/PhysRevE.92.031003`.

[30] I. Rubinstein and B. Zaltzman. "Electro-osmotically induced convection at a permselective membrane". In: *Physical Review E - Statistical Physics, Plasmas, Fluids, and Related Interdisciplinary Topics* 62.2 B (2000), pp. 2238–2251. DOI: `10.1103/PhysRevE.62.2238`.

[31] R. Kwak et al. "Microscale electrodialysis: Concentration profiling and vortex visualization". In: *Desalination* 308 (2013), pp. 138–146. DOI: `10.1016/j.desal.2012.07.017`.

[32] E. Güler et al. "Micro-structured membranes for electricity generation by reverse electrodialysis". In: *Journal of Membrane Science* 458 (2014), pp. 136–148. DOI: `10.1016/j.memsci.2014.01.060`.

[33] J. Balster, D. F. Stamatialis, and M. Wessling. "Membrane with integrated spacer". In: *Journal of Membrane Science* 360.1-2 (2010), pp. 185–189. DOI: `10.1016/j.memsci.2010.05.011`.

[34] Natalia D. Pismenskaya et al. "Evolution with Time of Hydrophobicity and Microrelief of a Cation-Exchange Membrane Surface and Its Impact on Overlimiting Mass Transfer". In: *The Journal of Physical Chemistry B* 116.7 (2012), pp. 2145–2161. DOI: `10.1021/jp2101896`.

[35] E. Korzhova et al. "Effect of surface hydrophobization on chronopotentiometric behavior of an AMX anion-exchange membrane at overlimiting currents". In: *Journal of Membrane Science* 500 (2016), pp. 161–170. ISSN: 0376-7388. DOI: `http://dx.doi.org/10.1016/j.memsci.2015.11.018`.

[36] Daniel C. Harris. *Quantitative Chemical Analysis*. New York: W.H. Freeman and Company, 2007. ISBN: 0-7167-7041-5.

[37] William M. Haynes, David R. Lide, and Thomas J. Bruno. *CRC handbook of chemistry and physics*. 2015. ISBN: 9781482260977.

[38] N. Nishad Fathima et al. "SPEEK polymeric membranes for fuel cell application and their characterization: A review". In: *Journal of Scientific and Industrial Research* 66.3 (2007), pp. 209–219.

[39] J. J. Krol. "Monopolar and bipolar ion exchange membranes". Thesis. Universiteit Twente, 1997.

[40] Joseph R. Lakowicz. *Principles of fluorescence spectroscopy*. 3rd ed. Singapore: Springer, 2006. ISBN: 0-387-31278-1.

[41] M.Y. Berezin and S. Achilefu. "Fluorescence lifetime measurements and biological imaging". In: *Chemical Reviews* 110.5 (2010), pp. 2641–2684. DOI: `10.1021/cr900343z`.

[42] W. Becker. "Fluorescence lifetime imaging - techniques and applications". In: *Journal of Microscopy* 247.2 (2012), pp. 119–136. DOI: `10.1111/j.1365-2818.2012.03618.x`.

[43] E.B. Van Munster and T.W.J. Gadella. "Fluorescence Lifetime Imaging Microscopy (FLIM)". In: *Advances in Biochemical Engineering/Biotechnology* 95 (2005), pp. 143–175. DOI: `10.1007/b102213`.

[44] Clara Druzgalski and Ali Mani. "Statistical analysis of electroconvection near an ion-selective membrane in the highly chaotic regime". In: *Phys. Rev. Fluids* 1 (7 Nov. 2016), p. 073601. DOI: `10.1103/PhysRevFluids.1.073601`.

[45] R.B. Bird, W.E. Stewart, and E.N. Lightfoot. *Transport Phenomena*. Wiley International edition. Wiley, 2007. ISBN: 9780470115398.

[46] E. Karatay et al. "Coupling between Buoyancy Forces and Electroconvective Instability near Ion-Selective Surfaces". In: *Physical Review Letters* 116.19 (2016). DOI: `10.1103/PhysRevLett.116.194501`.

[47] T. Xu. "Ion exchange membranes: State of their development and perspective". In: *Journal of Membrane Science* 263.1-2 (2005), pp. 1–29. DOI: `10.1016/j.memsci.2005.05.002`.

[48] R. Souzy and B. Ameduri. "Functional fluoropolymers for fuel cell membranes". In: *Progress in Polymer Science (Oxford)* 30.6 (2005), pp. 644–687. DOI: `10.1016/j.progpolymsci.2005.03.004`.

[49] R. Souzy, B. Ameduri, and B. Boutevin. "Synthesis and (co)polymerization of monofluoro, difluoro, trifluorostyrene and ((trifluorovinyl)oxy)benzene". In: *Progress in Polymer Science* 29.2 (2004), pp. 75–106. ISSN: 0079-6700. DOI: `10.1016/j.progpolymsci.2003.09.002`.

[50] O. Savadogo. “Emerging membranes for electrochemical systems: (I) solid polymer electrolyte membranes for fuel cell systems”. In: *Journal of New Materials for Electrochemical Systems* 1.1 (1998), pp. 47–66.

[51] G. Merle, M. Wessling, and K. Nijmeijer. “Anion exchange membranes for alkaline fuel cells: A review”. In: *Journal of Membrane Science* 377.1-2 (2011), pp. 1–35. DOI: `10.1016/j.memsci.2011.04.043`.

[52] P Atkins and J de Paula. *Physical Chemistry*. 11th ed. Oxford: Oxford University Press, 2010. ISBN: 978-0-19-954337-3.

[53] R Myers. *The Basics of Chemistry*. Westport: Greenwood Publishing Group, Inc., 2003. ISBN: 0-313-31664-3.

[54] L Coury. “Conductance Measurements Part 1: Theory”. In: *Current Separations* 18.3 (1999).

A | Ion-exchange membranes

Section 2.1.3 briefly discusses ion-exchange membranes (IEMs) since they are an essential part of electrodialyis. This appendix gives some examples of the types of IEMs: (1) cation-exchange membranes, (2) anion-exchange membranes and (3) bipolar membranes.[1]

A.1 Cation-exchange membranes

Cation-exchange membranes (CEMs) should be permeable for positive ions only and therefore contain negatively charged fixed-groups. In most of the cases, sulphonic acid groups provide the negative charge. They are almost completely dissociated over the whole pH-range and therefore classified as strong ion-exchange group.[47]

The difference between CEMs is the polymer matrix. Fluorinated ionomer membranes have been commercialized since the 1960's under tradenames as Nafion®[48], Dow®[49] and Flemion®[50] (Figure A.1a, Figure A.1b, Figure A.1c, respectively). These membranes have a very high chemical and thermal stability. Also partially fluorinated membranes have been synthesized (Figure A.1f), these are based on (non-fluorinated) styrene-divinylbenzene membranes (Figure A.1e). A problem with the latter one, is the oxidative depolymerization and therefore the fluorinated alternative is developed.[13, 50]

The fluorinated membranes are relatively expensive and therefore membranes based on polysulfone are considered (Figure A.1d). These are widely used in ultrafiltration and gas separation. By introducing a functionalized group in one of aromatic moieties it might be suitable for electrodialysis as well. The drawback of polysulfone based membranes is the tendency to swell relatively strong in water, which increases the resistance.[13]

Other examples of CEMs are partially sulphonated poly (ether ether ketone) membranes (SPEEK), polybenzimidazole based IEMs, polyimide based IEMs, polyphosphazene IEMs and styrene/ethylene- butadiene/styrene triblock copolymers.[13, 38]

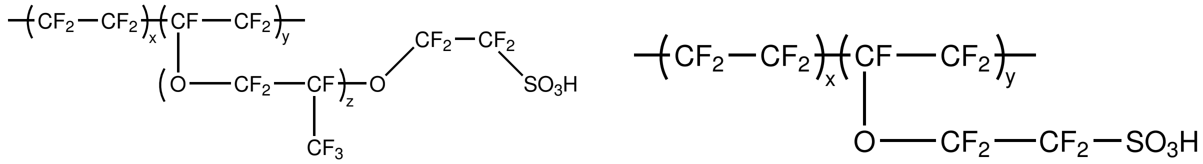

(a) Nafion® CEM. $x = 6 - 10, y = z = 1$.

(b) Dow® CEM. $x = 3 - 10, y = 1$.

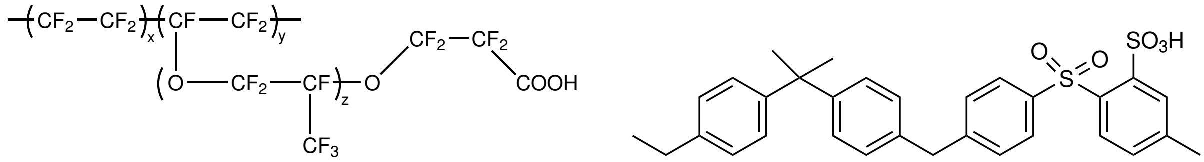

(c) Flemion® CEM. $x = 6 - 8, y = 0 - 1, z = 1$. Carboxyl acids carry the fixed negative charge.

(d) Polysulfone based CEM.

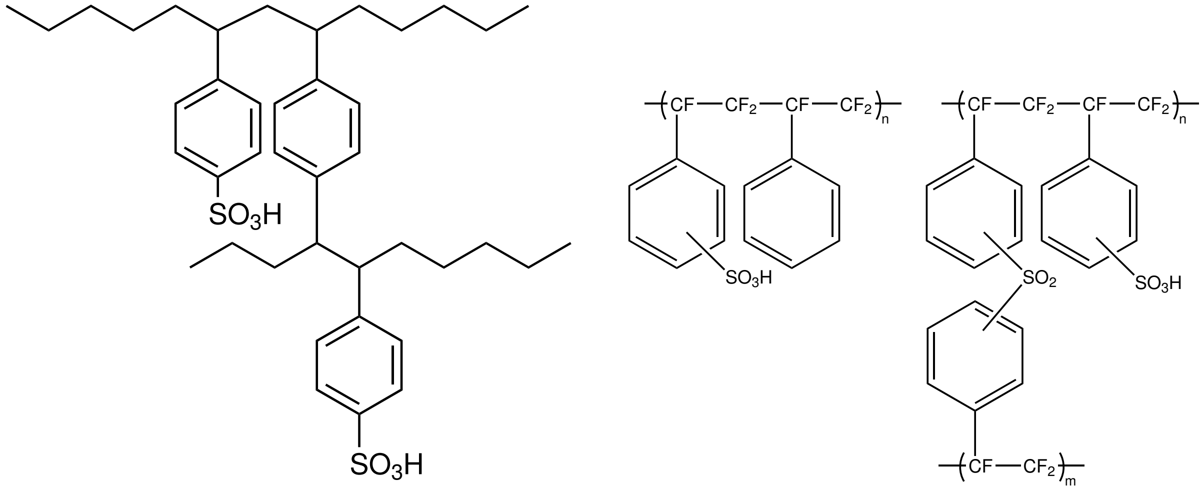

(e) Styrene-divinylbenzene based CEM.

(f) Partially fluorinated CEM. On the left a linear polymer and on the right a crosslinked polymer.

Figure A.1 – Exampels of cation-exchange membranes.[13, 48–50]

A.2 Anion-exchange membranes

Anion-exchange membranes (AEMs) are only permeable for negatively charged species and therefore contain fixed positive charges in the polymer structure. For strong AEMs, quaternary amide groups are responsible for the fixed charge since they are able to dissociate over almost the complete pH range. The polymer matrix is usually similar to that of a CEM, only the fuctionalized groups are different.

A few examples are given in Figure A.2.[13, 51]

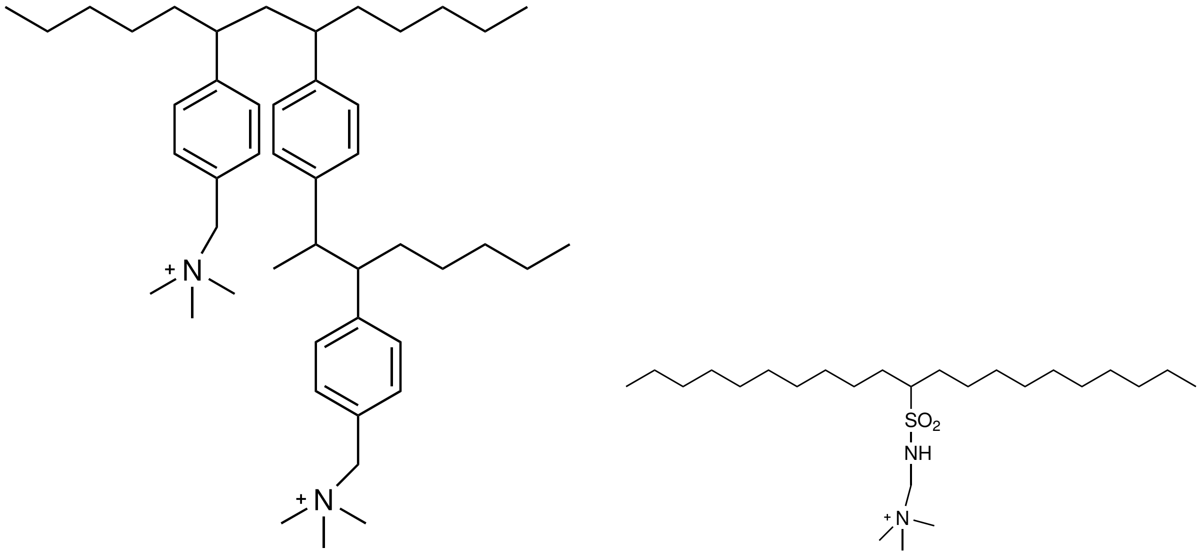

(a) Styrene-divinylbenzene based AEM.

(b) Polyethylene based AEM.

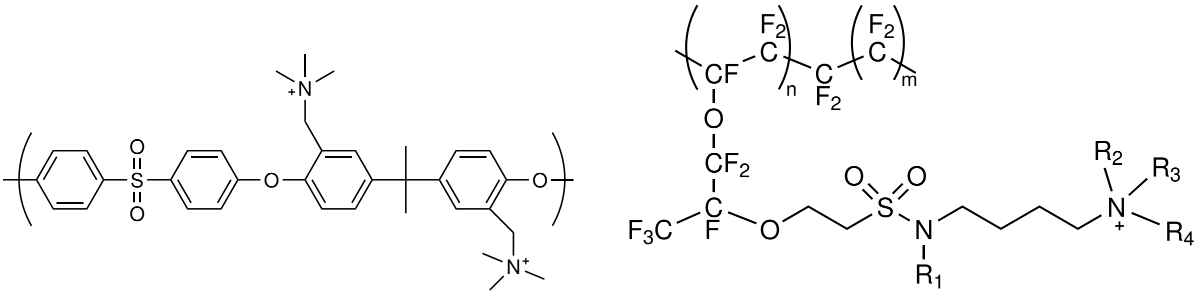

(c) Quaternized polyether sulfone based AEM.

(d) Sulphonic Nafion® based AEM.

Figure A.2 – Examples of anion-exchange membranes.[13, 51]

A.3 Bipolar membranes

Bipolar membranes contain both a cation and anion-exchange membrane. The production of acids and bases from their corresponding salts and the production of ultra-pure water are the major applications using bipolar membranes. In either of these applications, their ability to split water been the motivation to use these kind of membranes. Therefore, water-splitting capability is an additional criterion for the production of bipolar membranes.[1, 13]

Sulphonic acid and quaternary amide groups are responsible for the fixed charges in respectively CEMs and AEMs. Weaker ion-exchange groups are not completely dissociated in a mobile ion and fixed charge. It was shown that these groups catalyse water dissociation. Therefore they are introduced in the contact region of the membranes. Examples are carboxylic acids, phosphoric acid and tertiary or secondary amines.[13]

B | Conductivity calibration curve

The resistance of a system can be determined with electrochemical measurements. Conductivity (κ) and resistance (ρ) are related following eq. (B.1).

$$\kappa = \frac{1}{\rho} \tag{B.1}$$

The conductivity of an electrolyte solution depends on the concentration of the electrolyte. Therefore it is possible to determine the electrolyte concentration from the measured resistance. Calibration samples are prepared (0.5 to 20 mM $CuSO_4$) and the conductivity and temperature are measured with a WTW Cond3310 conductometer in fivefold. A power function ($f(x) = ax^b$) is fitted to the data points and the result is given in Figure B.1. The best fit is obtained using $a = 0.2431 \pm 0.0044$ and $b = 0.7818 \pm 0.0068$.

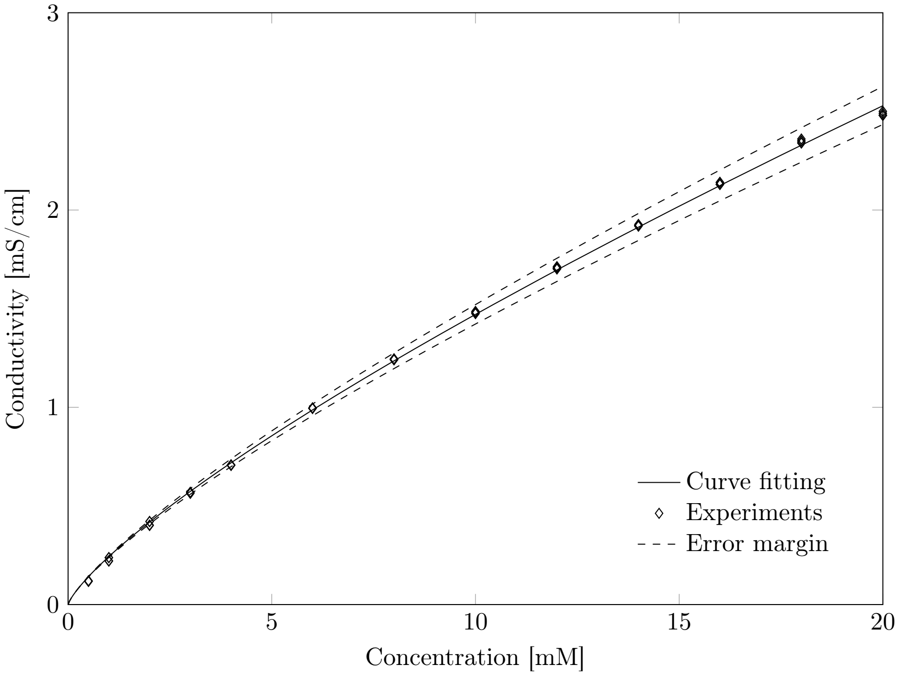

Figure B.1 – Calibration curve with 95 % confidence interval. The data is fitted to a one-term power function, $f(x) = ax^b$ with $a = 0.2431 \pm 0.0044$ and $b = 0.7818 \pm 0.0068$.

Another approach is to use the molar conductivity (Eq. (B.2)). Kohlrausch proposed a non-linear relation between concentration and conductivity following Eq. (B.3). This only holds for strong electrolytes, i.e. salts that are fully dissociated, at low concentration.[52]

$$\Lambda_m = \frac{\kappa}{c} \tag{B.2}$$

$$\Lambda_m = \Lambda_m^0 - K\sqrt{c} \tag{B.3}$$

$CuSO_4$ is a strong electrolyte and therefore obeys Kohlrausch's law.[53] Plotting the molar conductivity against the square root of the concentration should give a linear line with slope K, the Kohlrausch coefficient, and an offset equal to the limiting molar conductivity. After substituting eq. (B.2) in eq. (B.3) and rewriting, an explicit function for the conductivity as function of concentration can be obtained (eq. (B.4)).

$$\kappa = \Lambda_m^0 c - Kc^{1.5} \tag{B.4}$$

Figure B.2 shows the results obtained using Kohlrausch's law. Figure B.2a gives the linearization including 95 % confidence boundaries. This gives a limiting molar conductivity of 246.2 Scm^2/mol, whereas the literature value gives about 267 Scm^2/mol.[54] Eq. (B.4) is plotted in Figure B.2b to obtain a calibration curve of conductivity as function of concentration.

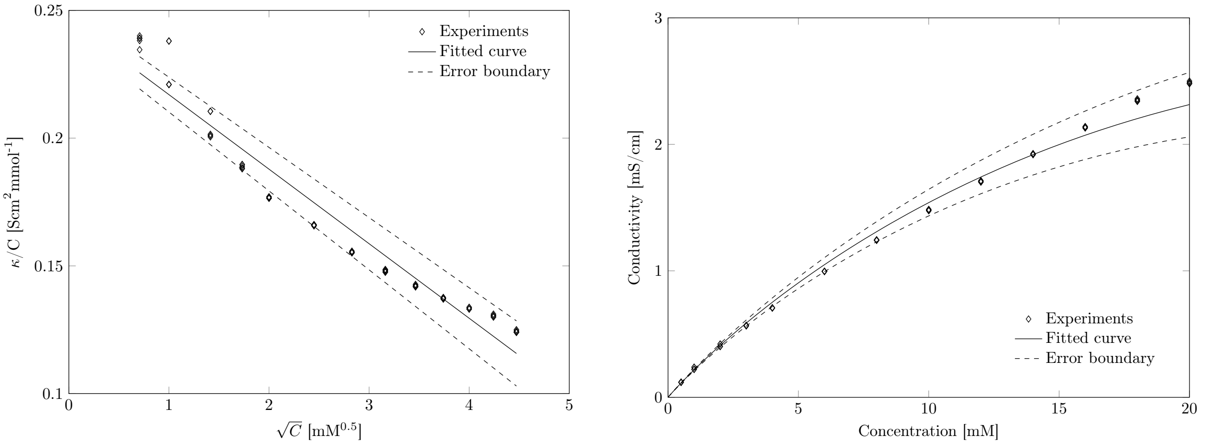

(a) Plot of the linearization eq.((B.3)). The best fit has a Λ_m^0 of 246.2 Scm^2/mol and K of 0.0292.

(b) Calibration curve of conductivity versus $CuSO_4$ concentration using linearization.

Figure B.2 – Calibration curve of conductivity as function of concentration using linearization of Kohlrausch's law.

The calibration curve obtained via data fitting shows a better agreement with the experimental data compared to the Kohlrausch's law approach as is shown in Figure B.3. Also the confidence intervals are smaller. Therefore, this curve will be used to determine the $CuSO_4$ concentration from the measured conductivity or resistance.

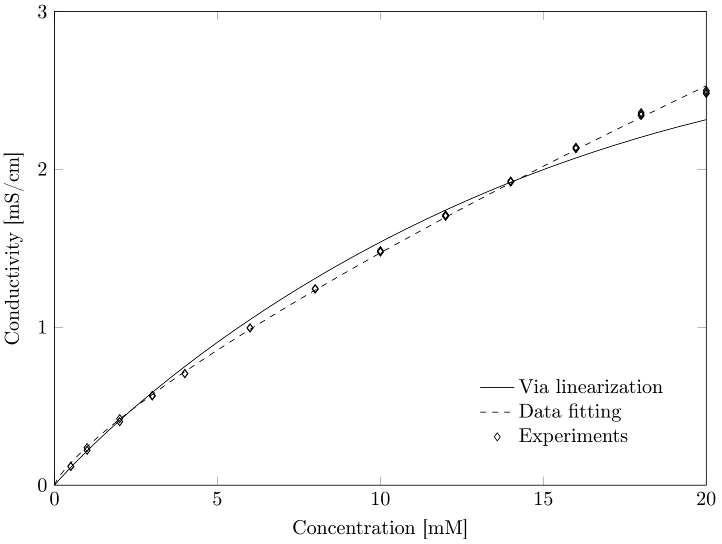

Figure B.3 – Comparison of the calibration curve using data fitting and Kohlrausch's Law.

C Nernst-Planck equation

In this appendix, the Nernst-Planck equation will be derived. Eq. (C.1) gives the Nernst-Planck equation, which describes mass transfer of ions in an electrolyte solution. There are multiple methods to derive this equation. In section C.1 the Maxwell-Stefan equation is the starting point of the derivation and in section C.2 a combination of driving forces is use to describe the system.

$$\mathbf{J}_i = \underbrace{-D_i \nabla c_i}_{\text{Diffusion}} \underbrace{- \frac{z_i D_i F}{RT} c_i \nabla \phi}_{\text{Migration}} + \underbrace{c_i \mathbf{u}}_{\text{Convection}} \tag{C.1}$$

C.1 Maxwell-Stefan

The Maxwell-Stefan equation describes the movement of species influenced by interactions with all other species. As a starting point, the force balance on a single species can be written as:

$$\text{driving force on species } i = \text{friction forces with other species } j \tag{C.2}$$

The driving force in this system is a gradient in electrochemical potential, $\tilde{\mu}_i$. It consists of the chemical potential, μ_i and the electrical potential, ϕ.

$$\tilde{\mu}_i = \mu_i + z_i F \phi \tag{C.3}$$

The chemical potential can be written as:

$$\mu_i = \mu_i^0 + V_i P + RT \ln a_i \tag{C.4}$$

Substitution of eq. (C.4) into eq. (C.3) gives eq. (C.5).

$$\tilde{\mu}_i = \mu_i^0 + V_i P + RT \ln a_i + z_i F \phi \tag{C.5}$$

The driving force on species i is the gradient of the electrochemical potential (with a minus sign as the movement will be against the gradient), which gives eq (C.6) This is the LHS of eq. (C.2).

$$\mathbf{F}_i = -RT \nabla \ln a_i - z_i F \nabla \phi - V_i \nabla P \tag{C.6}$$

The friction between species i and other species j is proportional to the velocity difference and the amount of species j. The friction coefficient, ζ_{ij}, relates the variables to the friction force.

$$\mathbf{F}_i = \sum_{\substack{j=1\\ j\neq i}}^{n} \zeta_{ij} x_j (\mathbf{u}_i - \mathbf{u}_j) \tag{C.7}$$

When there are four species in the system other than i, this becomes eq. (C.8). For a complete description, the same equation has to be set up for the four other species as well.

$$\mathbf{F}_i = \zeta_{i1} x_1 \left(\mathbf{u}_i - \mathbf{u}_1\right) + \zeta_{i2} x_2 \left(\mathbf{u}_i - \mathbf{u}_2\right) + \zeta_{i3} x_3 \left(\mathbf{u}_i - \mathbf{u}_3\right) + \zeta_{i4} x_4 \left(\mathbf{u}_i - \mathbf{u}_4\right) \tag{C.8}$$

Substituting eq. (C.7) into the RHS of eq (C.2) gives the Maxwell-Stefan equation for ion transport.

$$-RT\nabla \ln a_i - z_i F \nabla\phi - V_i \nabla P = \sum_{\substack{j=1\\ j\neq i}}^{n} \zeta_{ij} x_j \left(\mathbf{u}_i - \mathbf{u}_j\right) \tag{C.9}$$

The friction coefficient can be replaced by the Maxwell-Stefan diffusion coefficient, $\zeta_{ij} = {}^{RT}/_{Đ_{ij}}$, and the velocity by the flux, $\mathbf{J}_i = c_i \mathbf{u}_i = x_i c_t \mathbf{u}_i$.

$$-RT\nabla \ln a_i - z_i F \nabla\phi - V_i \nabla P = \sum_{\substack{j=1\\ j\neq i}}^{n} \frac{RT}{Đ_{ij}} \left(\frac{x_j \mathbf{J}_i}{c_t x_i} - \frac{\mathbf{J}_j}{c_t}\right) \tag{C.10}$$

After some rewriting this will become eq. (C.11)

$$x_i \nabla \ln a_i + \frac{x_i z_i F}{RT} \nabla\phi + \frac{x_i V_i}{RT} \nabla P = \sum_{\substack{j=1\\ j\neq i}}^{n} \frac{x_i \mathbf{J}_j - x_j \mathbf{J}_i}{Đ_{ij} c_t} \tag{C.11}$$

The Nernst-Planck equation is a simplification of the Maxwell-Stefan equation. The assumption is that the pressure gradient is negligible in electrolyte systems.

$$x_i \nabla \ln a_i + \frac{x_i z_i F}{RT} \nabla\phi = \sum_{\substack{j=1\\ j\neq i}}^{n} \frac{x_i \mathbf{J}_j - x_j \mathbf{J}_i}{Đ_{ij} c_t} \tag{C.12}$$

The activity can be written as $a_i = \gamma_i c_i$, where γ_i is the activity coefficient. This corrects for non-idealities in the system. Here, a very dilute system is assumed, which has some consequences:

- the activity coefficient becomes 1 (eq. (C.13)),
- there are only ion-water frictions (eq. (C.14)),
- the water fraction can be assumed as 1 (eq. (C.15)),
- the Maxwell-Stefan diffusion coefficient becomes the binary diffusion coefficient, $Đ_{ij} = D_i$ (eq. (C.16)).

$$x_i \nabla \ln c_i + \frac{x_i z_i F}{RT} \nabla \phi = \sum_{\substack{j=1 \\ j \neq i}}^{n} \frac{x_i \mathbf{J}_j - x_j \mathbf{J}_i}{Đ_{ij} c_t} \tag{C.13}$$

$$x_i \nabla \ln c_i + \frac{x_i z_i F}{RT} \nabla \phi = \frac{x_i \mathbf{J}_w - x_w \mathbf{J}_i}{Đ_{ij} c_t} \tag{C.14}$$

$$x_i \nabla \ln c_i + \frac{x_i z_i F}{RT} \nabla \phi = \frac{x_i \mathbf{J}_w - \mathbf{J}_i}{Đ_{ij} c_t} \tag{C.15}$$

$$x_i \mathbf{J}_w - \mathbf{J}_i = D_i c_i \nabla \ln c_i + \frac{z_i D_i F}{RT} c_i \nabla \phi \tag{C.16}$$

Applying the chain rule gives that $\nabla \ln c_i = \frac{1}{c_i} \nabla c_i$ and the Nernst-Planck equation becomes:

$$x_i \mathbf{J}_w - \mathbf{J}_i = D_i \nabla c_i + \frac{z_i D_i F}{RT} c_i \nabla \phi \tag{C.17}$$

The final step is to replace the water flux with the water velocity, $\mathbf{J}_w = \mathbf{u}_w x_w c_t = \mathbf{u} c_t$. This gives the final Nernst-Planck equation derived from the Maxwell-Stefan equation given in eq. (C.18). The first term on the RHS is mass transport by diffusion under influence of a concentration gradient. The second term is ion migration due to an (externally) imposed electric field. The final term is a convection term.

$$\mathbf{J}_i = \underbrace{-D_i \nabla c_i}_{\text{Diffusion}} \underbrace{- \frac{z_i D_i F}{RT} c_i \nabla \phi}_{\text{Migration}} + \underbrace{c_i \mathbf{u}}_{\text{Convection}} \tag{C.18}$$

C.2 Driving forces

The flux of an ion in an electrolyte can be seen as a combination of fluxes. In electrodialysis, three forms of mass transport can be identified, namely:

1. Convection – mass transport due to movement of the fluid. Usually caused by a pressure difference,
2. Diffusion – mass transport due to a gradient in chemical potential and
3. Migration – transport of ions due to a gradient in electrical potential.

In general the concentration change of a species can be described with:

$$\frac{\partial c_i}{\partial t} = -\nabla \cdot \mathbf{J}_i + p \tag{C.19}$$

In the domain of interest there is assumed to be no production, p, of species i. This might not be completely true for H^+ and OH^- due to possible water splitting.

$$\frac{\partial c_i}{\partial t} = -\nabla \cdot \mathbf{J}_i \tag{C.20}$$

C.2.1 Convection

Convection is mass transport due to the movement of the fluid in which the species are present. Therefore the flux is in the same direction as the fluid velocity.

$$\mathbf{J}_{i,conv} = c_i\mathbf{u} \tag{C.21}$$

C.2.2 Diffusion

Diffusion is the movement of molecules due to a gradient in chemical potential. This can be a gradient in pressure or in concentration, of which concentration is the most dominant term. Diffusion due to a concentration gradient can be described by Fick's law, eq (C.22).

$$\mathbf{J}_{i,diff} = -D_i\nabla c_i \tag{C.22}$$

C.2.3 Migration

Charged species also move under the influence of an electric field. The driving force is then a gradient in electrical potential. This can be caused by e.g. a wall charge or an externally applied potential. The flux of due to this ion migration is described by eq. (C.23).

$$\mathbf{J}_{i,migr} = -M_i c_i\nabla\phi \tag{C.23}$$

Here, M_i is the mobility of the ions and is related to the diffusion coefficient following the Einstein equation.

$$D_i = \frac{M_i k_B T}{e z_i} \tag{C.24}$$

With, $k_B = {}^{R}/_{N_{av}}$ and $F = eN_{av}$, the mobility of the ions can be written as:

$$M_i = \frac{z_i D_i F}{RT} \tag{C.25}$$

Substution of eq. (C.25) into eq. (C.23) gives the expression for flux through migration.

$$\mathbf{J}_{i,migr} = -\frac{z_i D_i F}{RT}c_i\nabla\phi \tag{C.26}$$

C.2.4 Total flux

The total flux of species i is the sum of the three individual fluxes.

$$\mathbf{J}_i = \mathbf{J}_{i,diff} + \mathbf{J}_{i,migr} + \mathbf{J}_{i,conv} \tag{C.27}$$

Substituting eq. (C.22), (C.26) and (C.21) into (C.27) gives the Nernst-Planck equation describing the flux of ions.

$$\mathbf{J}_i = \underbrace{-D_i \nabla c_i}_{\text{Diffusion}} - \underbrace{\frac{z_i D_i F}{RT} c_i \nabla \phi}_{\text{Migration}} + \underbrace{c_i \mathbf{u}}_{\text{Convection}} \tag{C.28}$$

D | Plateau length

The plateau length is an important parameter to investigate electrochemical processes using ion-exchange membranes. Experiments determining the i-V curve and chronoamperometry are combined to determine the plateau length. Then also the limiting current density and onset of overlimiting current (OLC) can be determined. Figure D.1 shows the experimental data. For each region of the i-V curve (Ohmic, plateau and OLC), a linear line is drawn. At the lowest and highest potentials of the i-V curve, the system reaches equilibrium. This can be used to draw the lines for the Ohmic and OLC regime. Chronoamperometry measurements are used to determine the slope of the plateau region.

The intersect of the Ohmic and plateau lines correspond to the limiting current density, whereas the intersect of the plateau and OLC lines give the onset of the OLC. For a flat membrane and 100 µm structured membrane this can be done without problems, while for the 200 and 800 µm structured membranes this is more difficult.

For the 200 µm structured membrane it seems possible to draw a line for every region. However, the plateau line and OLC line do not intersect. Looking at the i-t data (Figure D.2), it shows that only at a low potential, equilibrium is reached and not in the OLC region. Therefore, the slope of the OLC region cannot be fitted to the data, but has to be lower.

Chronoamperometry data for the 800 µm structured membrane does not show a plateau. The equilibrium current density obtained for 0.8 V and 1 V with chronoamperometric measurements are similar to the current density obtained from the i-V curve. However, the i-V data is not yet at equilibrium, which indicates that the chronoamperometry data does not give the correct values. Figure D.3 shows the i-t data of all experiments at 1 V. The current density fluctuates and does not reach a steady-state, where a smooth decay, as in Figure 3.4b, is expected. A reason could be that these data are the last experiments with the membrane and that the membrane is damaged over time. Therefore the plateau line is drawn assuming the data points for 0.8 V and 1 V are at a similar current density as for 0.6 V. Table D.1 gives the results using the above described method.

Table D.1 – The plateau length, limiting current density and slope of the i-V curve in the three region of the graph.

Membrane	**Plateau length [V]**	i_{lim} [A/m^2]	**Slope** [S/m^2]		
			Ohmic	***Plateau***	***OLC***
flat	0.94	2.7	17.8	2.6	4.3
100 µm	0.70	3.1	17.9	1.7	3.4
200 µm	0.65	2.4	10.7	1.3	2.4
800 µm	1.18	4.0	13.3	1.0	2.9

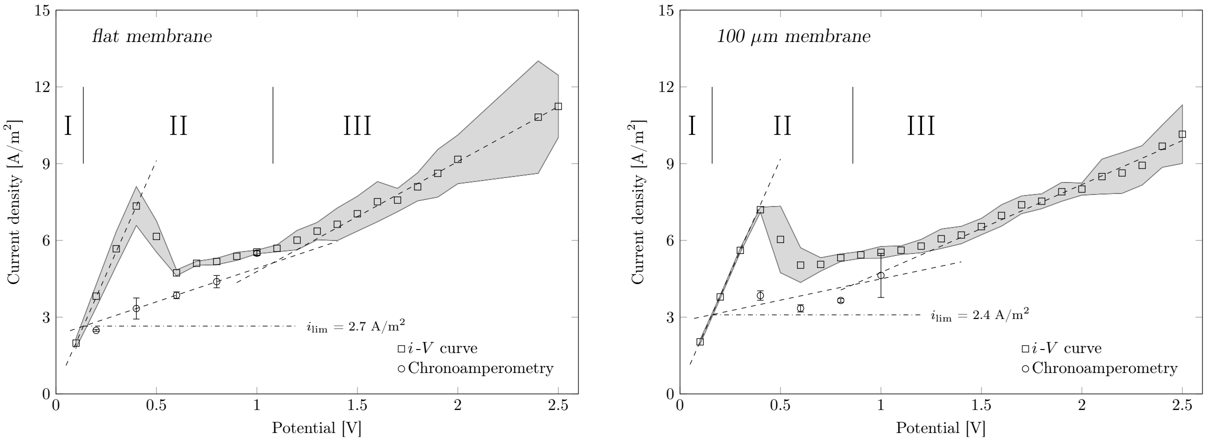

(a) Flat membrane

(b) 100 µm structured membrane

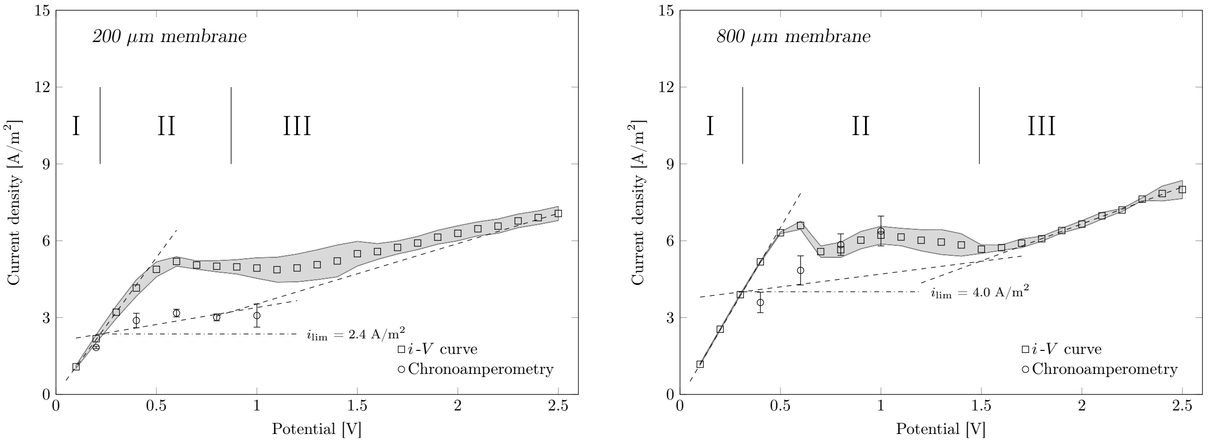

(c) 200 µm structured membrane

(d) 800 µm structured membrane

Figure D.1 – Determination of (I) Ohmic region, (II) plateau region and (III) OLC region.

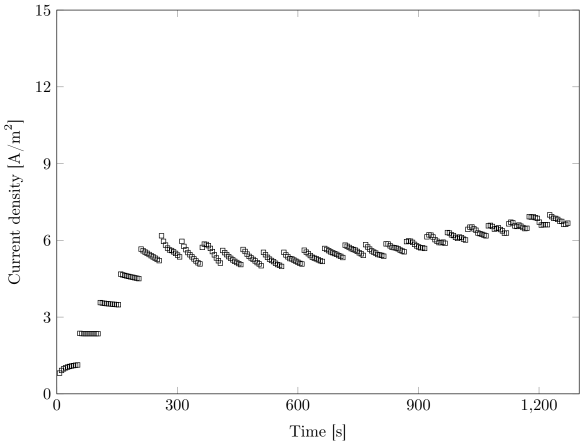

Figure D.2 – i-V curve of a 200 µm structured membrane.

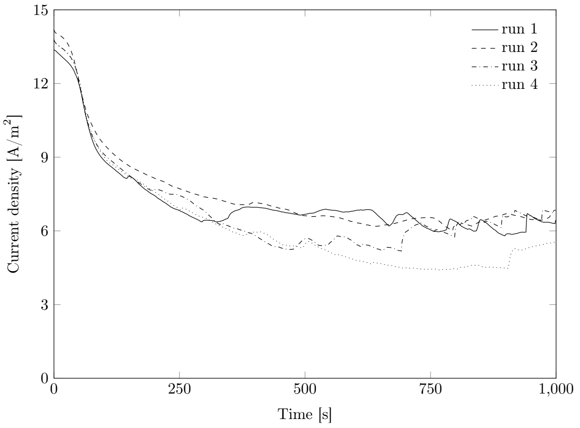

Figure D.3 – Chronoamperometry measurements for a 800 µm structured membrane at 1 V

E | Chronoamperometry data

Figure E.1 contains the i-t data from chronoamperometry measurements. At $t = 0$, a potential of 0.4 to 1 V is applied and the current response is measured for 1000 s. For all applied potentials, the different structured membranes are compared. The average of multiple runs is calculated, including the standard deviation, this is shown in the graphs. The shaded areas represent the standard deviation.

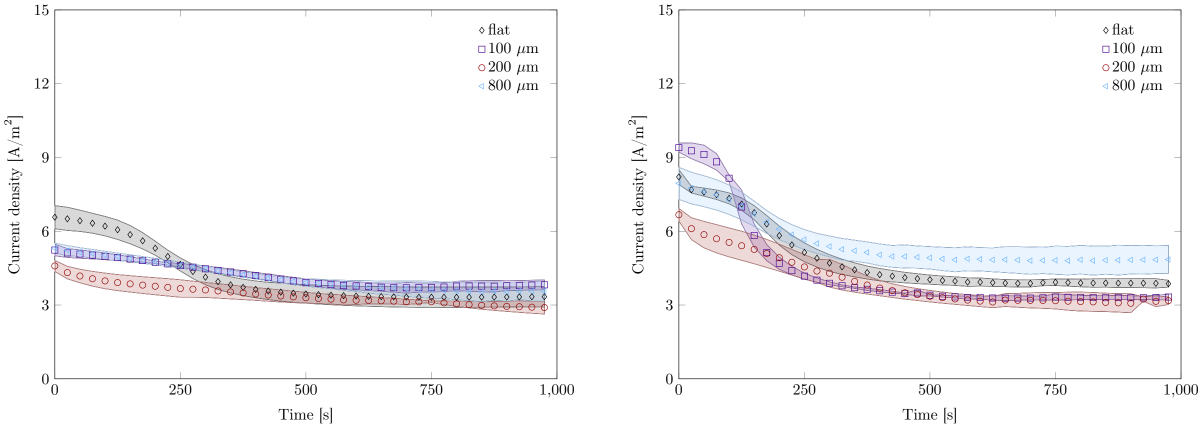

(a) $\Delta\phi = 0.4$ V.

(b) $\Delta\phi = 0.6$ V.

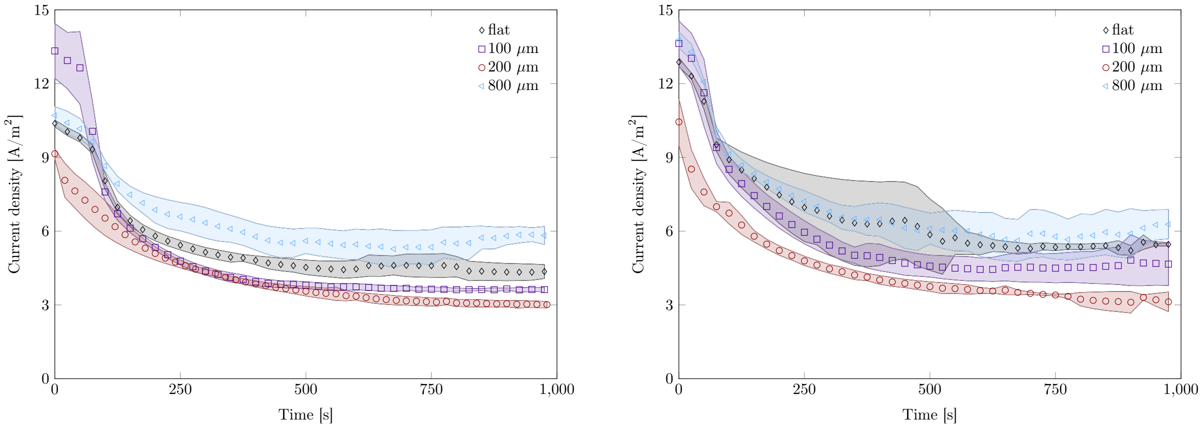

(c) $\Delta\phi = 0.8$ V.

(d) $\Delta\phi = 1$ V.

Figure E.1 – i-t curves of chronoamperometry experiments using different applied potentials. The shaded regions represent the standard deviation.

Additional experiments at 0.2 V are carried out. This has only been done a flat membrane and a 200 µm structured membrane due to time limitations. The results are shown in Figure E.2.

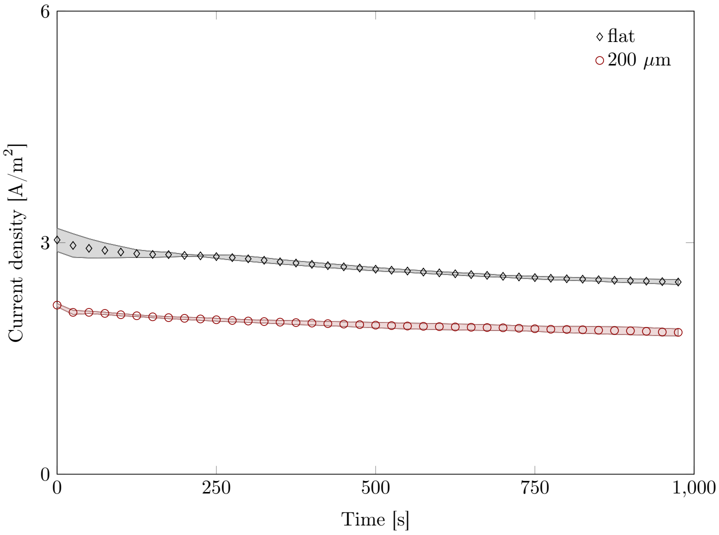

Figure E.2 – Chronoamperometry data at 0.2 V.

F | Numerical results

This appendix presents concentration profiles and velocity profiles obtained from 2D simulations. Simulations have been carried out for a flat, 100, 200, 400 and 800 µm structured membrane. The concentration profiles are for the copper concentration. This differs a bit from the sulfate concentration, however, this is not visible by the naked eye. Also numerical simulations have been obtained for membranes with a curved interface, this represents the bending of the membrane when it is placed inside the cell, these are given in Figures F.6, F.7 and F.8.

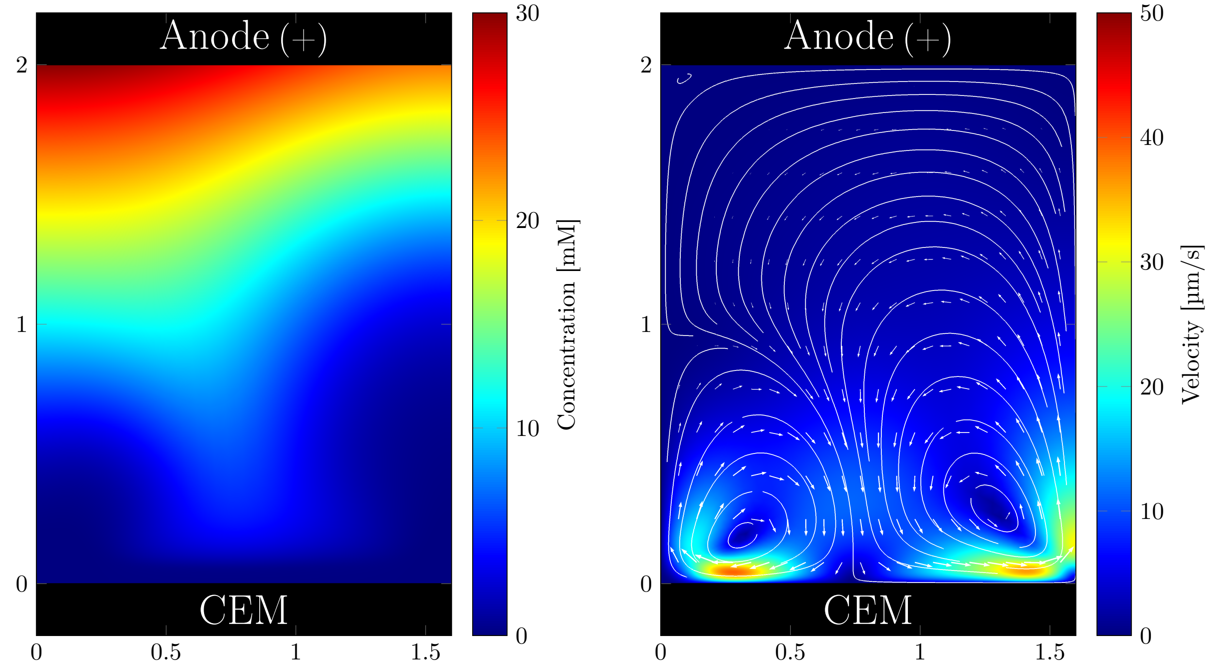

(a) Concentration profile.

(b) Velocity profile.

Figure F.1 – Simulation results for a flat membrane. A current density of 3.47 A/m^2 is obtained. The length scale is in mm.

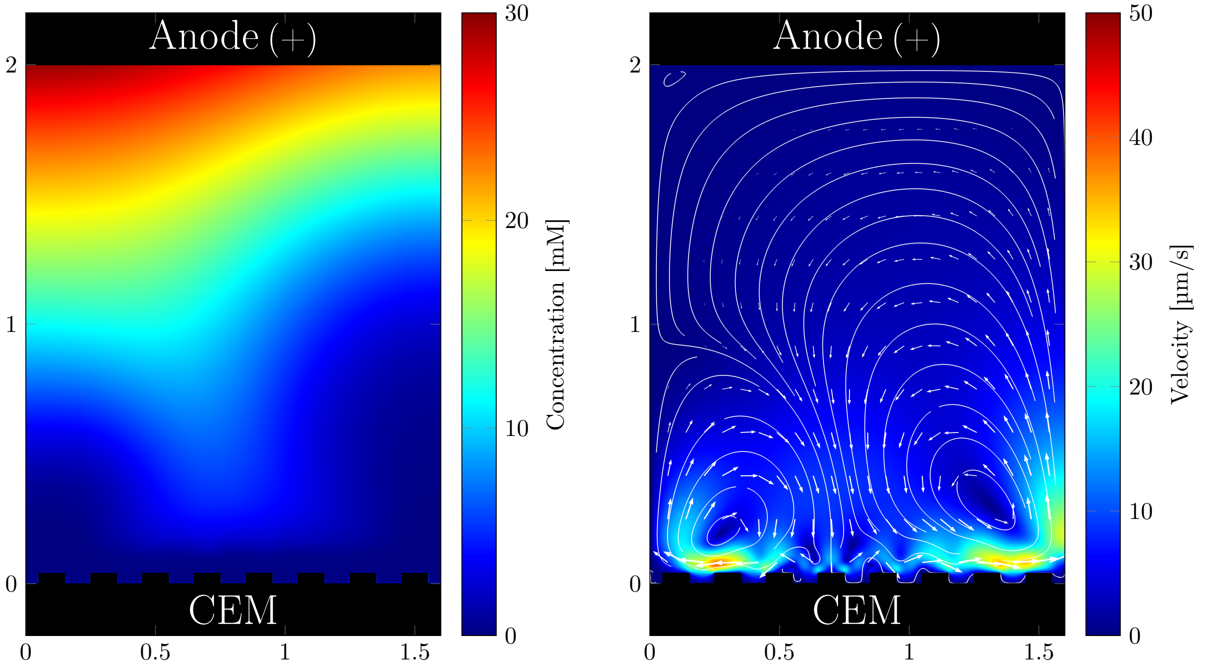

(a) Concentration profile.

(b) Velocity profile.

Figure F.2 – Simulation results for a 100 µm structured membrane. A current density of 3.39 A/m^2 is obtained. The length scale is in mm.

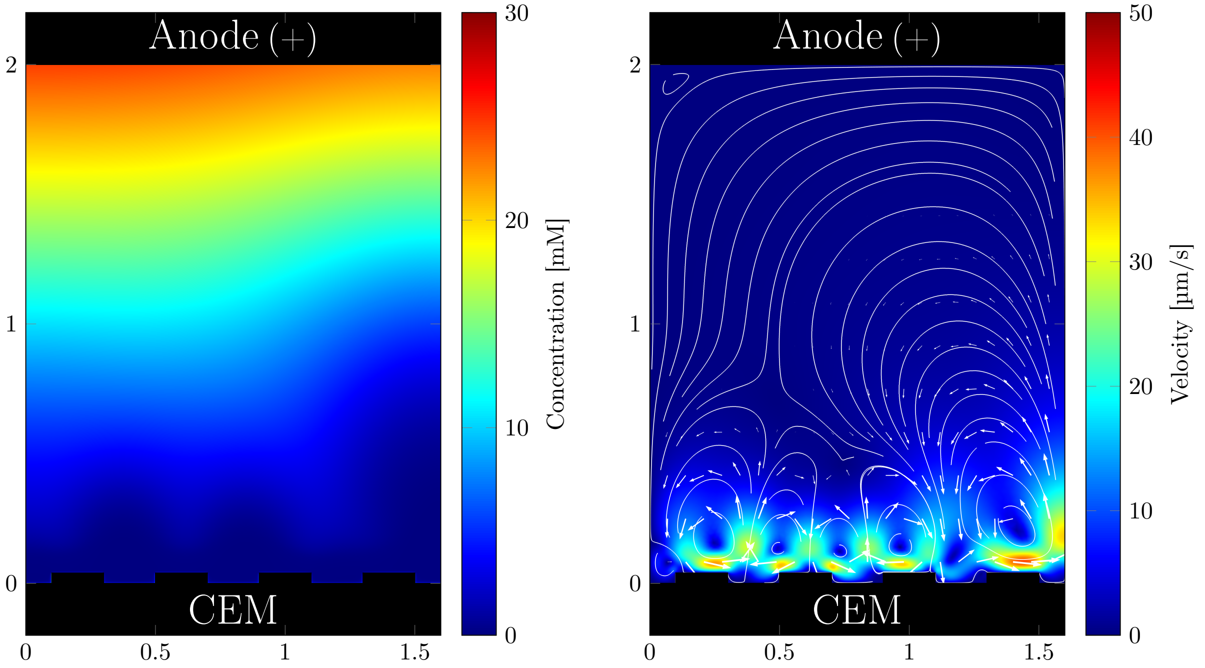

(a) Concentration profile.

(b) Velocity profile.

Figure F.3 – Simulation results for a 200 µm structured membrane. A current density of 2.62 A/m^2 is obtained. The length scale is in mm.

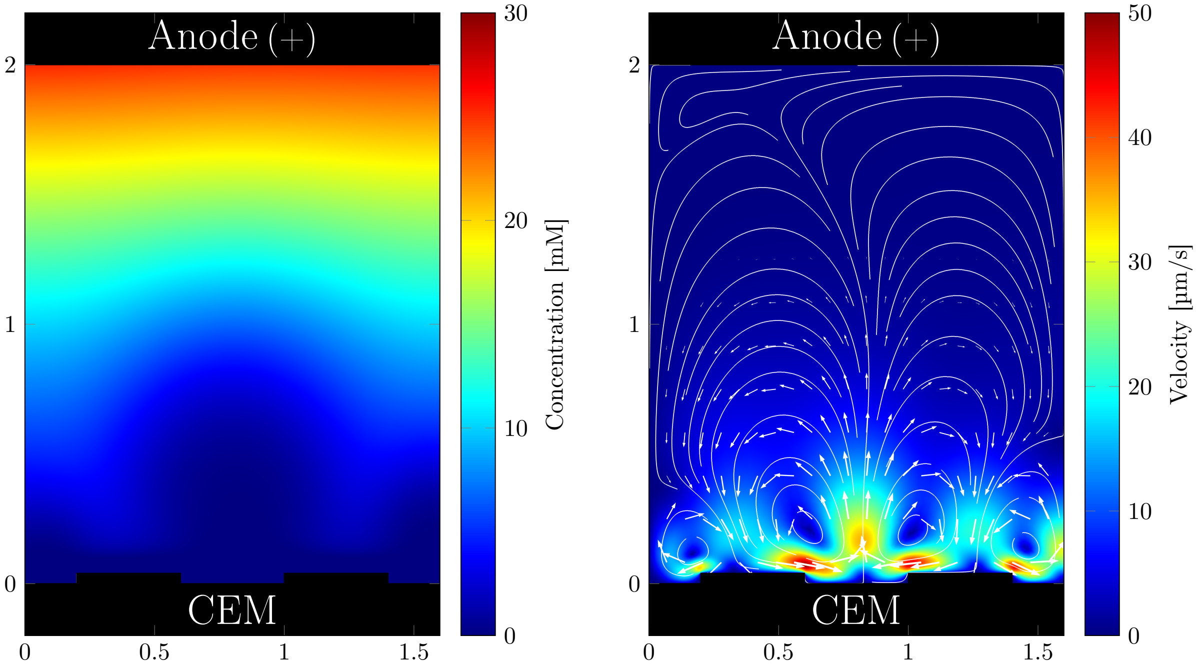

(a) Concentration profile.

(b) Velocity profile.

Figure F.4 – Simulation results for a 400 µm structured membrane. A current density of 2.72 A/m^2 is obtained. The length scale is in mm.

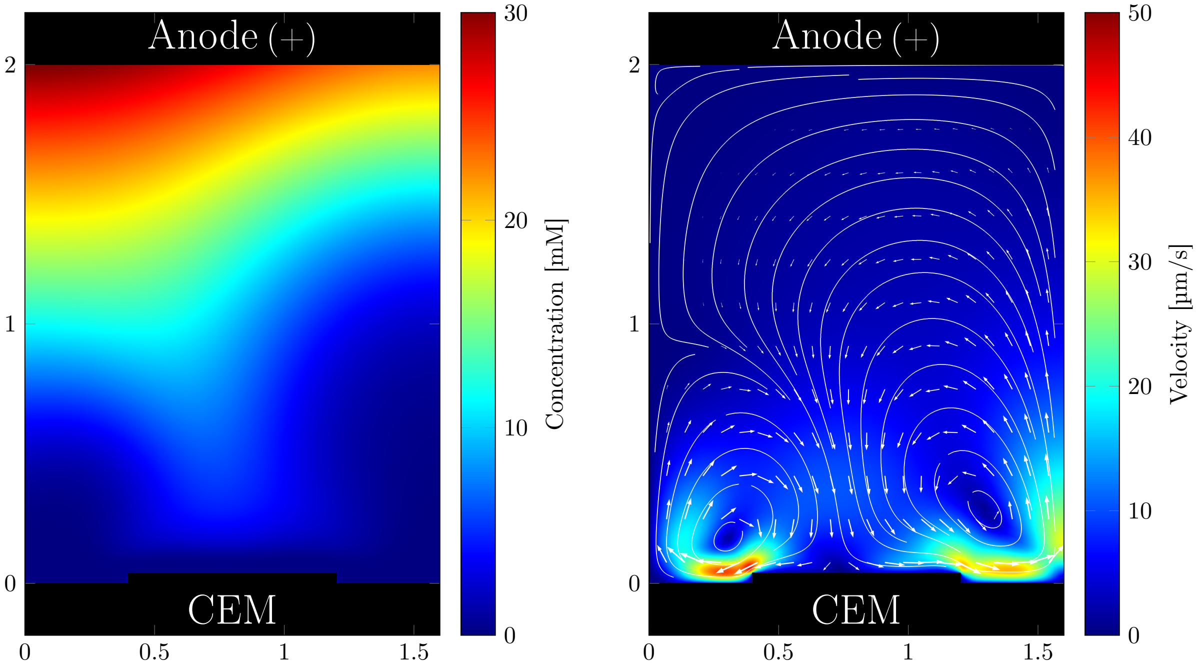

(a) Concentration profile.

(b) Velocity profile.

Figure F.5 – Simulation results for a 800 µm structured membrane. A current density of 3.57 A/m^2 is obtained. The length scale is in mm.

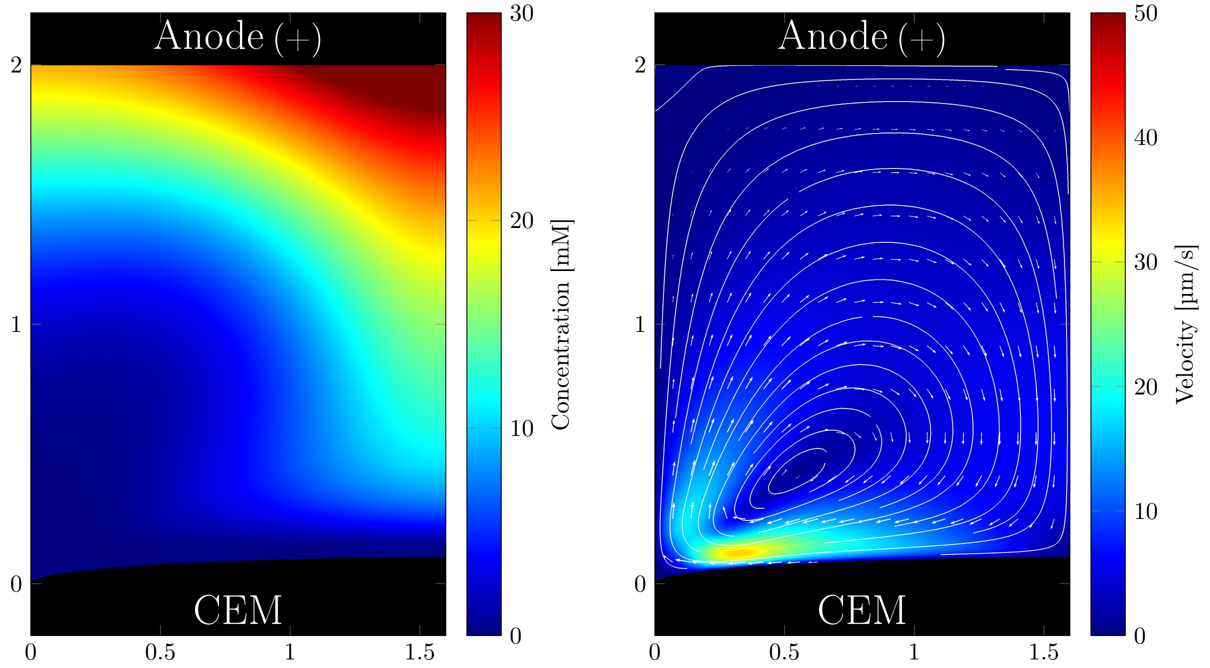

(a) Concentration profile.

(b) Velocity profile.

Figure F.6 – Simulation results for a slightly curved membrane surface, maximum height of the curvature is 0.1 mm. A current density of 4.50 A/m^2 is obtained. The length scale is in mm.

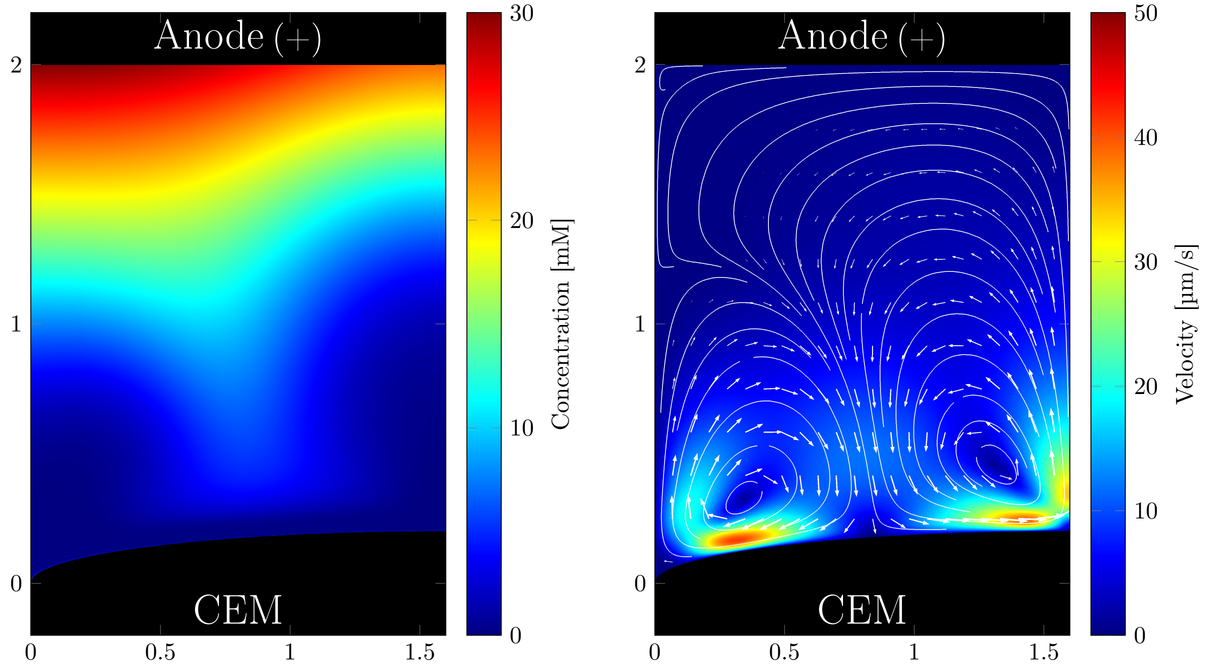

(a) Concentration profile.

(b) Velocity profile.

Figure F.7 – Simulation results for an intermediate curvature of the membrane surface, maximum height of the curvature is 0.2 mm. A current density of 3.87 A/m^2 is obtained. The length scale is in mm.

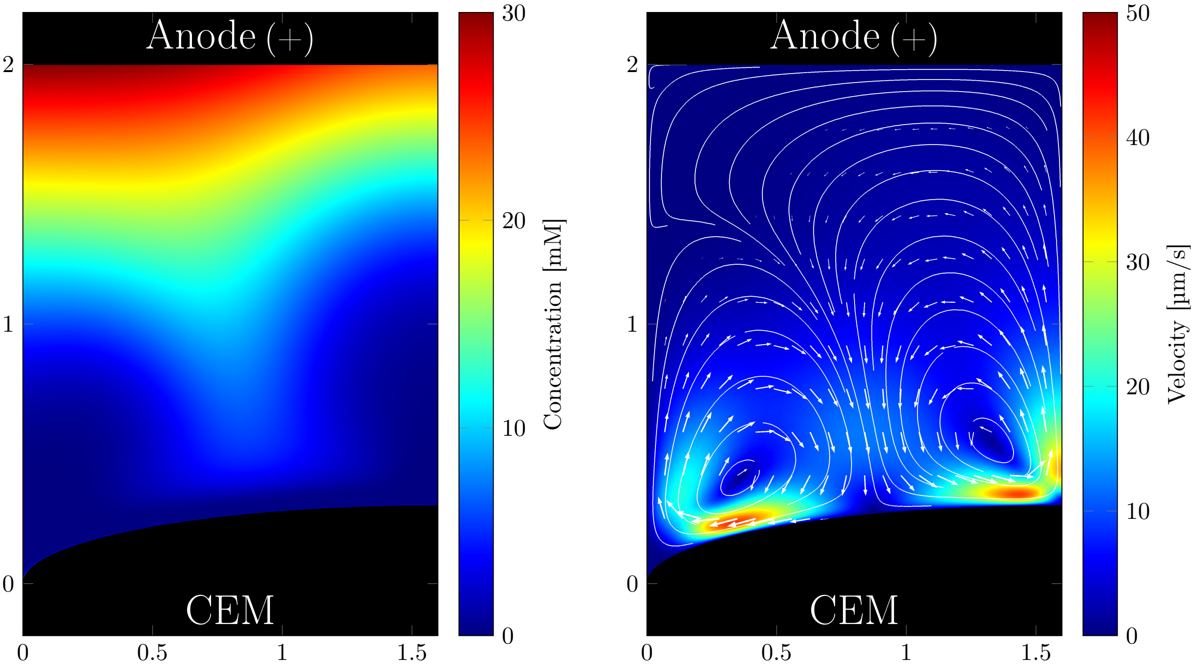

(a) Concentration profile.

(b) Velocity profile.

Figure F.8 – Simulation results for a highly curved membrane surface, maximum height of the curvature is 0.3 mm. A current density of 4.15 A/m^2 is obtained. The length scale is in mm.

G | FLIM images

This appendix shows the concentration profiles for the different membranes with an Alexa Fluor® 488 concentration of 2.5 µM and 5 µM. Profiles are shown at the beginning of the experiment ($t = 0\,\mathrm{s}$) and near the end ($t = 900\,\mathrm{s}$). Chronoamperometry are carried out at a potential difference of 1 V.

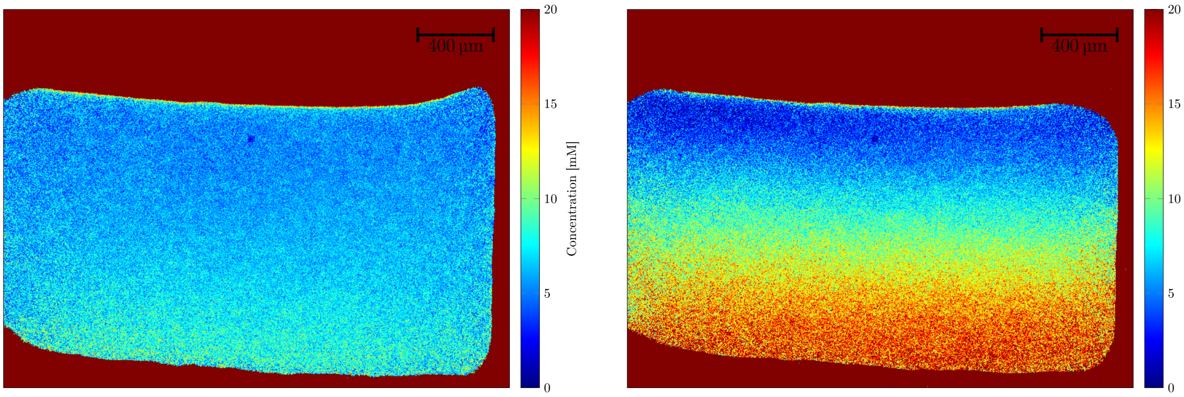

(a) Concentration profile at $t = 0\,\mathrm{s}$ with an Alexa Fluor® 488 concentration of 2.5 µM.

(b) Concentration profile at $t = 900\,\mathrm{s}$ with an Alexa Fluor® 488 concentration of 2.5 µM.

Figure G.1 – Concentration profiles obtained with FLIM for a flat membrane for different points in time.

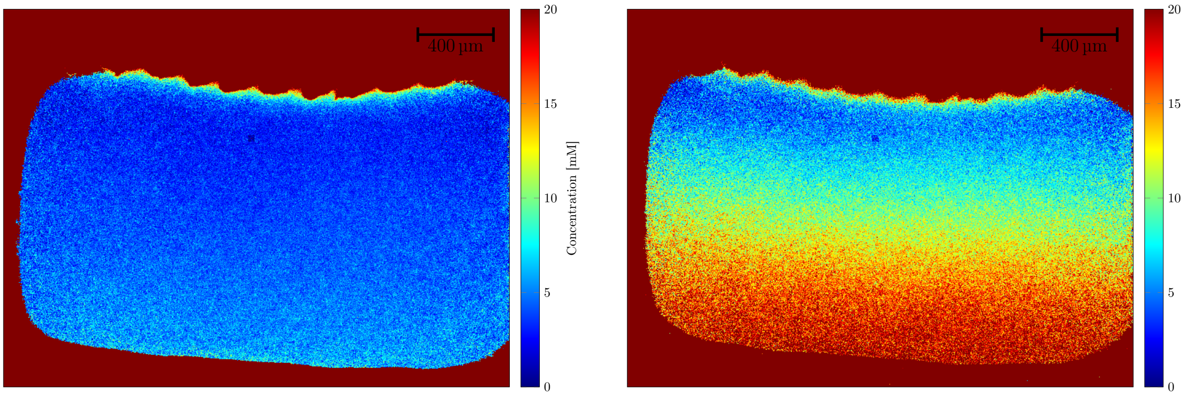

(a) Concentration profile at $t = 0\,\mathrm{s}$ with an Alexa Fluor® 488 concentration of 2.5 µM.

(b) Concentration profile at $t = 900\,\mathrm{s}$ with an Alexa Fluor® 488 concentration of 2.5 µM.

Figure G.2 – Concentration profiles obtained with FLIM for a 100 µm structured membrane for different points in time.

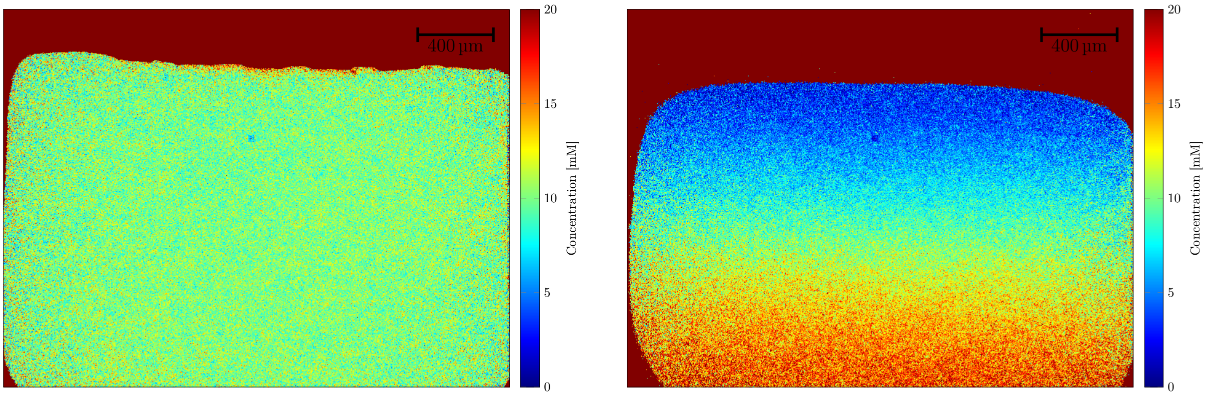

(a) Concentration profile at $t = 0\,\mathrm{s}$ with an Alexa Fluor® 488 concentration of 2.5 µM.

(b) Concentration profile at $t = 900\,\mathrm{s}$ with an Alexa Fluor® 488 concentration of 2.5 µM.

Figure G.3 – Concentration profiles obtained with FLIM for a 200 µm structured membrane for different points in time.

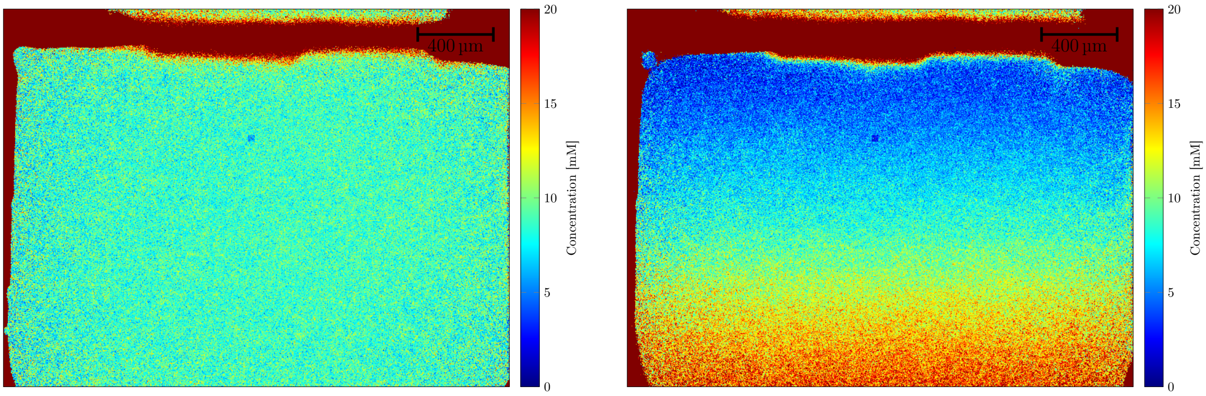

(a) Concentration profile at $t = 0\,\mathrm{s}$ with an Alexa Fluor® 488 concentration of 2.5 µM.

(b) Concentration profile at $t = 900\,\mathrm{s}$ with an Alexa Fluor® 488 concentration of 2.5 µM.

Figure G.4 – Concentration profiles obtained with FLIM for a 800 µm structured membrane for different points in time.

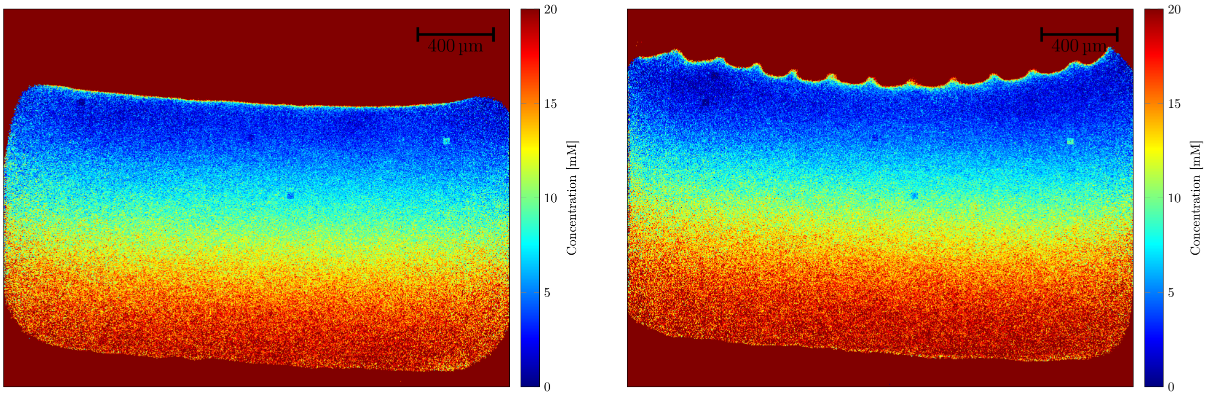

(a) Concentration profile for a flat membrane.

(b) Concentration profile for a 100 µm structured membrane.

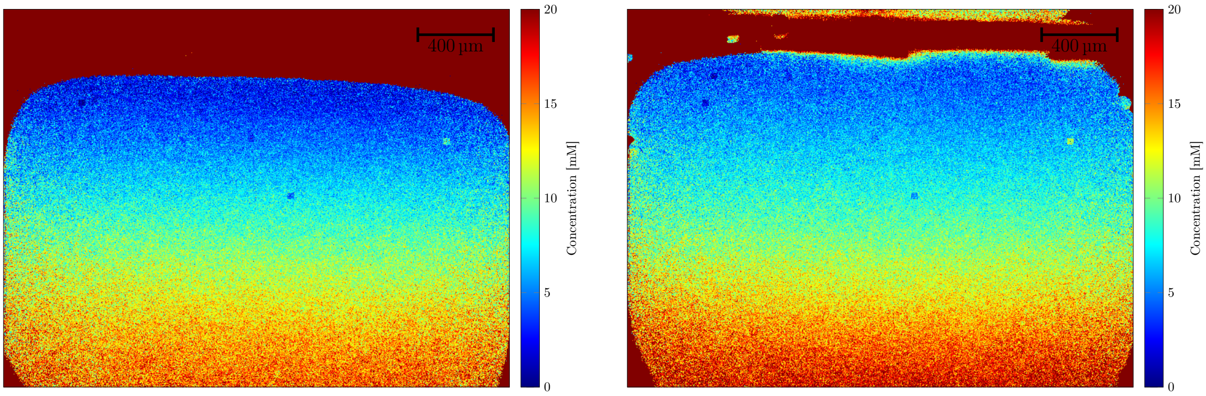

(c) Concentration profile for a 200 µm membrane.

(d) Concentration profile for a 800 µm structured membrane.

Figure G.5 – Concentration profiles obtained with FLIM at $t = 900\,\mathrm{s}$ with a 5 µM Alexa Fluor® 488 concentration showing no significant improvement compared to 2.5 µM.